Reservoir Geomechanics and Casing Stability, X1-3Area, Daqing Oilfield

by

Hongxue Han

A thesis
presented to the University of Waterloo
in fulfillment of the
thesis requirement for the degree of
Master of Science
in
Earth Sciences

Waterloo, Ontario, Canada, 2006

AUTHOR'S DECLARATION FOR ELECTRONIC SUBMISSION OF A THESIS

I hereby declare that I am the sole author of this thesis. This is a true copy of the thesis, including any required final revisions, as accepted by my examiners.

I understand that my thesis may be made electronically available to the public.

Abstract

It is widely understood that injection and production activities can induce additional stress fields that will couple with the *in situ* stress field. An increased shear stress may cause serious casing stability issue, and casing integrity is one of the major issues in the development of an oilfield. In this thesis, I will present a methodology for semi-quantitatively addressing the physical processes, the occurrence, and the key influential factors associated with large-area casing shear issues in Daqing Oilfield. In the research, I will investigate reservoir heterogeneity and the far-field stress field in the Daqing Oilfield, China; I will review fundamental theories of rock strength, rock failure, casing shear, and techniques for coupling fluid flow and mechanical response of the reservoirs; and I will present mathematical simulations of large-area casing shear in one typical area (X1-3B) in Daqing Oilfield, under different regimes of water-affected shale area ratio and block pressure difference.

Heterogeneity in Daqing Oilfield varies according to the scale. Mega-heterogeneity is not too serious: the geometry of the oilfield is simple, the structure is flat, and faults are numerous and complex, but distributed evenly. Macro-heterogeneity is, however, intense. Horizontal macro-heterogeneity is associated with lateral variations because of different depositional facies. Vertical macro-heterogeneity of Daqing Oilfield because of layering is typified by up to 100 individual sand layers with thickness ranging from 0.2 to 20 m and permeability ranging from 20 to 1600 mD (average 230 mD). Furthermore, there are a number of stacked sand-silt-shale (clastic lithofacies) sequences. Mercury porosimetry and photo-micro-graphic analyses were used to investigate the micro-heterogeneity of Daqing Oilfield. This method yields a complete pore size distribution, from several nanometers to several thousands of micro-meters as well as cumulative pore volume distributions, pore-throat aspect ratios, and fractal dimensions. The fractal dimension can be used to describe the heterogeneity at the pore scale; for sandstones, the larger the fractal dimension of a specific pore structure, the more heterogeneous it is. Reservoir sandstones of Daqing Oilfield have similar porosity and mineralogy, so their micro-heterogeneity lies in a micro-

structure of considerable variability. Differences in micro-structure affect permeability, which also varies considerably and evidences a considerable amount of micro-scale anisotropy. Finally, the number and nature of faults in the oilfield make the macro-scale heterogeneity more complex.

Rock strength is affected by both intrinsic factors and external factors. Increased water saturation affects rock strength by decreasing both rock cohesion and rock friction angle. In Daqing Oilfield, is seems that a 5% increase of water content in shale can decrease the maximum shearing resistance of shale by approximately 40%.

Hysteretic behavior leads to porosity and permeability decreases during the compaction stage of oilfield development (increasing σ'). Also, injection pressures are inevitably kept as high as possible in the pursuit of greater production rates. These lead to non-homogeneous distributions of pressures as well as in changes of material behavior over time.

Loss of shear strength with water content increase, inherent reservoir heterogeneity, and long periods of high-pressure water injection from a number of wells are three key factors leading to casing shear occurring over large areas in Daqing Oilfield. Reservoir heterogeneity and structural complexity foster uneven formation pressure distribution, leading to inter-block pressure differences. Sustained long-term elevated pressures affect overburden shale mechanical strength as well as reducing normal stresses, and the affected area increases with time under high-pressure injection so that the affected areas overlap at the field scale and alter the *in situ* stress field. Once the maximum compressive stress parallels or nearly parallels the differential pressure, and the water-affected shale area is big enough, the shear stability of the interface between the shale and the sandstone is severely compromised, and when the thrust stress imposed exceeds the shearing resistance, the strata will slip in a direction corresponding to the vector from high-pressure to low-pressure areas. The change in this slip and creep displacement field is the major reason for the serious casing deformation damage in Daqing Oilfield.

To quantify the scale effect of the water-affected shale area on casing stability, coupled non-linear poroelastic fluid flow was simulated for a typical area. The Daqing Oilfield

simulation result is in coincidence with the *in situ* observation of disturbed stress fields and casing displacement. The water-affected area has a scale effect on the casing stability. The ratio of the water-affected shale formation area to the total area influences the stability coefficient much more than the block pressure difference. In the studied area, under conditions of injection pressure of 12.7 MPa and no more than 2.5 MPa block pressure difference, the water-affected ratio should be smaller than 0.50 or so in order to maintain areal casing stability. By history matching, in the studied area under current development condition and considering the water-affected ratio, so long as the injection pressure and pressure differential between blocks are controlled to be less than 12.7 MPa and 0.86 MPa respectively, formation shear slip along a horizontal surface will no longer occur.

Acknowledgements

This thesis would not be complete without acknowledgement of the efforts of those people who helped throughout this research.

First I would like to thank my supervisor, Prof. Maurice B. Dusseault, for his consistent technical, moral, and financial support. His efforts, enthusiasm, and encouragement motivated the author throughout the study.

I also would like to thank my co-supervisor, Marios A. Ioannidis, for his technical instruction about this research.

A lot of thanks are given to Ioannis Chatzis, Edison S. Amirtharaj, and Giriga Padhy. I appreciate their help in the lab.

I am also grateful to Dr. Baoci Xu, for his effort to help me get the chance to continue my study, for his generous help and assistance during the whole period while I studied on campus.

Special thanks are given to the members of my MSc committee, Prof. M.B. Dusseault, and Prof. Marios A. Ioannidis, and Prof. Stephen G. Evans, for their technical help during my study, and for their critical reviews and useful suggestions on this thesis.

I am very thankful to my colleagues at Daqing Oilfield Company Ltd., China. In particular, I would like to thank my oilfield supervisor, Dr. Yupu Wang, for his consideration of my career path, and Dr. He Liu, for his continued care, help, and encouragement.

I would like to thank my wife Bo Peng and my son Roc Han who made all of this possible with their unconditional love and sacrifice. Their arms are always open to me whether I succeed or fail. I am in debt to my parents and my younger brother Hongbo Han, for their unconditioned love, encouragement, and financial assistance.

Table of Contents

List of Figures

List of Tables

Chapter 1
Introduction

Casing stability is one of the major issues associated with development of an oilfield. Induced stress fields arising from production and injection activities have a great influence on the *in situ* stress field. Specific heterogeneous reservoir geological characteristics make the situation even more complex. All these issues have triggered extensive studies in geomechanics and casing stability.

1.1 Problem Statement

Wellbore stability is one of the major problems associated with and caused by large-scale withdrawal or injection of fluids. Loss of wells due to severe casing damage can be costly. By the end of 2004, the cumulative number of wells in Daqing Oilfield (Heilongjiang Province, PRC) showing casing shear reached 18.77% of total wells (most of the wells exhibiting casing shear are concentrated in seven areas), and the annual economical loss from casing shear is more than $125 million (Liu *et al*. 2005).

Various mechanisms for casing damage are recognized, including compression, tension, and shear (Fredrich *et al*. 2000). Compressional failures can occur within the producing interval due to large vertical strains associated with compaction. Tensile failures can result when material outside of the compacting zone provides vertical support to material above the compacting zone (arching). Thermal expansion due to steam injection may also contribute to development of tensile stresses in the overburden as well as to shear stresses at lithological interfaces (sand-shale usually). Shear failures can be induced by horizontal displacements along the flanks of a subsidence bowl or by localized slip along weak bedding planes or reactivated faults in the overburden above the reservoir.

Causes of casing loss in Daqing Oilfield are somewhat more complex because of its high degree of heterogeneity. There are up to 100 individual sand layers with thickness

ranging from 0.2 meters to 20 meters. These layers are mainly sandstone or siltstone with a porosity range from 20% to 30% (average 25%) and a permeability range from 20 to 1600 mD (average 230 mD, Osmar *et al.* 1990). After years of research work and field investigations in Daqing Oilfield, it was concluded that there were two main reasons for casing failure. One reason appeared to be that injected water invades into mudstones and shale and decreases the shear strength and friction coefficient; as a result, creep deformation will take place under ambient and induced differential stresses. The second reason was that unbalanced water injection causes significant reservoir pressure differences, which are of course accompanied by strains (He *et al.* 2005). When the pressure differences were large enough, casing shear would occur through the accumulation of deformation along an interface. Unfortunately, these studies initially were based on qualitative interpretation, and no quantitative analyses for the causes have been reported.

For many years, attempts have been made to mitigate the casing shear problem; various repair and work-over technologies have been developed (Lan *et al.* 2000 and He *et al.* 2005). However, these are mainly work-over or repair techniques for single wells intended to also effect pressure control measures for wells in sand bodies. Nothing has been reported quantitatively about the extent of the water-affected area and the possibility of establishing pressure difference limits over a large region. Although repair techniques are successful for single wells, the total percentage of casing loss is still very high (see Figure 1-1).

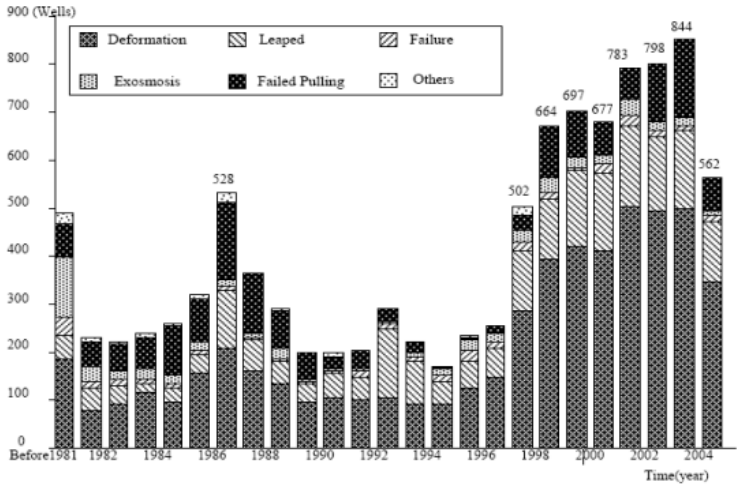

Figure 1-1: Casing Shear Occurrences in Daqing Oilfield From 1981 to 2004

(Peak of 844 shear events in 2003, After Liu *et al.* 2005)

1.2 Objectives of the Thesis

The overall objective is to analyze the physics of large-area casing shear and to develop a methodology to assess or predict the occurrence of large-area casing shear. Specifically, there are three main goals in this thesis:

1) To understand the mechanism of casing loss during the process of production from or injection into reservoirs;
2) To investigate heterogeneous rock properties of the area and the effects of pressure change, in order to analyze the slip mechanisms in the context of the *in situ* stress;
3) Based on experimental field studies of the influence of injection pressure on the injection-induced strain and displacement fields, simulate numerically deformation phenomena, and try to find out the technical limits (e.g. pressure limits) associated with the occurrence of severe casing deformation.

1.3 Location of the Study Area

Daqing Oilfield is located in the northeast of China; it is the biggest oilfield in China. The general geographic location and tectonic position is illustrated in this chapter. Its reservoir geology and production history is also introduced.

1.3.1 Geographic Location and Tectonic Position of Daqing Oilfield

Daqing Oilfield is located in Heilongjiang Province, which is a northeast province in China. It is adjacent to Jilin province, Inner Mongolia, Russia, and North Korea. The geological location of the oilfield is sketched in Figure 1-2.

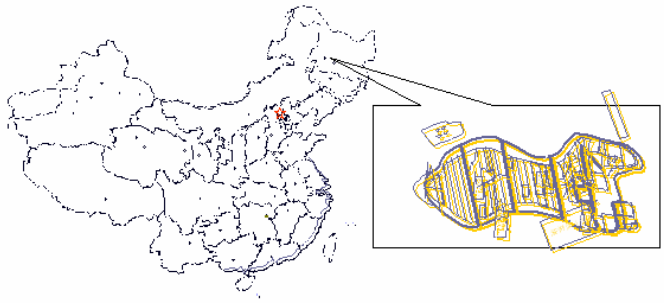

Figure 1-2: Geographical Location Map of Daqing Oilfield

Tectonically, Daqing Oilfield is in the middle of the depression of the Songliao Basin on a secondary structure belt. It is an elongated anticline with a surface area of around 11,000 km^2 (Wang *et al.* 1995). It is a so-called *placanticline*. The structure is quite flat with a distance of 117 km in the North-South direction and a distance of 6-23 km in the East-West direction. The anticline was formed under stress arising from a nearly east-west direction stress field. The direction of the maximum horizontal stresses, σ_H, is around N 80°E (Li *et al.* 1997 and Chen *et al.* 2002). Generally, below a certain depth (~500 m) in reservoirs in the Songliao Basin, the maximum horizontal stresses σ_H > vertical stress, and σ_v > the minimum stress, σ_h. The three stresses have the following relationship with depth *H* (Li *et al.* 1997).

$$\sigma_H = -2.342 + 0.026576H \qquad (1.1)$$

$$\sigma_h = -0.7765 + 0.01824H \quad (1.2)$$

$$\sigma_v = 0.021H \quad (1.3)$$

There are 7 local high points in this oilfield, each with its own name (see Figure 1-3). The study area in this thesis is in the middle of the oilfield, the northern Xingshugang area.

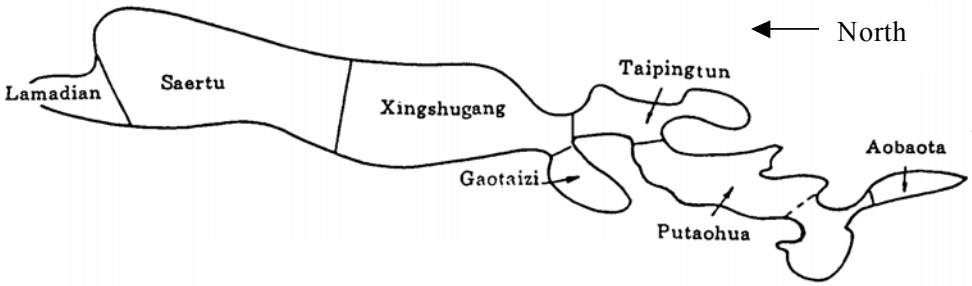

Figure 1-3: Position of Local High Points in Daqing Oilfield

(After Wang *et al.* 1995)

1.3.2 Reservoir Geology and Production History

Reservoirs in Daqing Oilfield are encountered at depths from 700 to 1200 m. Many different oil-bearing zones exist, and there is a high degree of heterogeneity. Oil zones are parts of a Lower Cretaceous, fluvio-deltaic sedimentary sequence that contains up to 100 individual sand layers with thickness ranging from 0.2 meters to 20 meters (Han 2006). Table 1-1 gives the statistics of reservoir zone thickness. These layers are mainly sandstone or siltstone with a porosity range from 20% to 30% (average 25%) and a permeability range from 10-20 to 1600-3000 mD (average 230 mD) (Osmar *et al.* 1990, Wang *et al.* 1995).

Table 1-1: Statistics on the Thickness of Different Types of Pay Zones

Type of Thickness	Very thick (>5.0m)	Thick (5.0-m-2.0m)	Medium (2.0m-0.5m)	Thin (0.5m-0.2m)	Ultra Thin (<0.2m)	Total
Thickness	10.3	13.0	36.7	12.6	14.1	86.7
%	12.5	15.7	44.4	11.2	16.2	100

(After Wang *et al.* 1995)

Daqing Oilfield was discovered in Sept. 1959 and was developed since 1960. The development of the reservoirs has undergone several stages (Wang *et al.* 1995, Li *et al.* 1995, and Wang *et al.* 2004). Shortly after the beginning of oilfield development, water was injected to sustain the formation pressure; by 1961, the entire oilfield was on water flood. Separate zonal injection and production strategies were used in the early 1960's to mitigate or cope with vertical heterogeneity. In 1964, the zonal distribution rate has reached up to 79.8%, with a water cut increase dropping from 14.8% to 1.81% during the low water cut period from 1964 to 1972. From 1976 to 1985, oil production was developed to over 5000×10^4 tonnes annually. This stable production was maintained thereafter until 2004 (see Figure 1-4). Oilfield overall water cut rate of 40-70% took place in this period. In the period from 1986 to 1995, a second ten-year stable production development phase was attained. At this time, major reservoir layers became watered out extensively; the production rate declined quickly as the water cut rose. The first well net infill drilling program was carried out in this period, and the annual oil production reached 5500×10^4 tonnes. After 1995, the oilfield was developed by a combination of water flooding and polymer flooding.

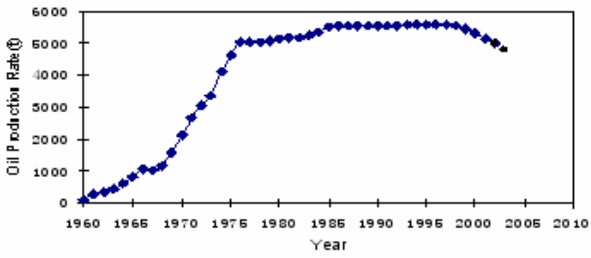

Figure 1-4: Yearly Oil Production Rate in Daqing Oilfield

(After Wang *et al.* 2004)

1.4 Structure of the Thesis

To address the problems associated with reservoir geomechanics and casing stability, this thesis is divided into six chapters.

This first chapter is a general overview of problems and a brief introduction to the Daqing Oilfield. In this chapter, the casing instability issue in Daqing Oilfield is outlined, the general purpose of the research is stated, and the position and the production history of Daqing Oilfield are briefly introduced. Also, a general qualitative description of the causes of large area casing shear is presented.

Chapter 2 introduces the fundamental theories related to casing shear. In this chapter, the concepts of effective stress are discussed; some important concepts and theories of rock strength, rock failure, and casing failure are studied in detail.

Chapter 3 discusses reservoir heterogeneity and effects of pressure change. In this chapter, mega-heterogeneity, macro-horizontal heterogeneity, macro-vertical heterogeneity, and micro-heterogeneity of reservoirs in Daqing Oilfield are discussed. A combination of mercury porosimetry and photo-micro-graphic analysis method is presented for pore structure characterization. Methods for micro-heterogeneity determination are presented and the phenomenon of pore structure parameters variation under pressure changes is introduced.

Chapter 4 reviews techniques for coupled geomechanics and fluid flow modeling, governing equations for fluid flow in deformable porous media, constitutive equations, and the finite element method for solving complex partial differential equations. The different coupling techniques are compared in this chapter.

Chapter 5 presents observations of *in situ* stress variations under injection pressure change and simulation of the influences of injection pressure changes on the stress field. The scale effects of the water-affected area ratio to the casing stability issue are simulated and analyzed in this chapter.

Chapter 6 contains the general conclusions and recommendation section.

Nomenclature used in the thesis is listed after Chapter 6.

References are listed in alphabetic sequence at the end of the thesis.

Chapter 2
Fundamental Theories of Casing Shear

2.1 Introduction

Casing shear is caused by rock shear and rock shear occurs when shear stress exceeds the rock strength. Petroleum recovery activities, such as injection and production, lead to pore pressure changes, which in turn influence porosity and stresses. Before discussing details of casing stability, some important concepts and theories of effective stress, rock strength, rock failure, and stress variation associated with petroleum production practices should be clarified and emphasized.

2.2 Theory of Effective Stress

To analyze stress/strain behavior and rock strength, we normally identify and estimate the three principal stresses: the major - σ_1 - intermediate -σ_2 - and minor - σ_3. It is assumed that the vertical stress - σ_v - is one of the principal stresses; therefore, the other two are the larger and smaller horizontal stresses, σ_H and σ_h, respectively. The natural shear stresses, τ, are highest on planes 45° from the principal-stress planes, and the maximum shear stress, τ_{max}, is defined as $(\sigma_1 - \sigma_3)/2$. Thus, the larger the natural difference in the major and minor principal stresses, the greater the shear stress, and the closer the rock is to a state of failure or shear slip (Dusseault, 2001).

The effective stresses are the differences between total stresses in the rock and pore pressure in the interconnected voids. The effective stress is defined by Terzaghi's law:

$$\sigma' = \sigma - \alpha p_f \qquad (2.1)$$

where σ is total normal stress; σ' is effective normal stresses; α is the Biot parameter (also called poroelastic constant); and p_f is pore pressure. Physically it means that the rock skeleton carries the part σ' of the total external stress σ , while the remaining part, αp_f, is carried by the fluid in the porous medium. The Biot parameter α takes into account the

compressibility of the mineral in addition to the bulk compressibility of the rock skeleton. Its range is from 0 to 1 with a low value for low porosity, very stiff reservoir rocks. For high porosity rocks such as the 20-30% porosity sandstone in Daqing Oilfield, the Biot parameter, α, can be assumed to be 1.0, in comparison to other effects (Dusseault 2005).

2.3 Rock Strength

Rock mechanical strength is the most crucial rock property in casing shear analysis and is the basis for stability analysis. Generally, rock strength is reported in four different manners: uniaxial compressive strength (UCS), shear strength, tensile strength, and residual strength (after shearing has destroyed all cohesion).

Figure 2-1 illustrates typical rock response to external uniaxial stress (Han 2003). UCS is the peak stress that rock can sustain during a uniaxial compression test with no lateral confinement. Usually, it is treated as a benchmark for rock stability analysis because it is easy to measure. The higher the UCS value, the more stable rocks are assumed to be.

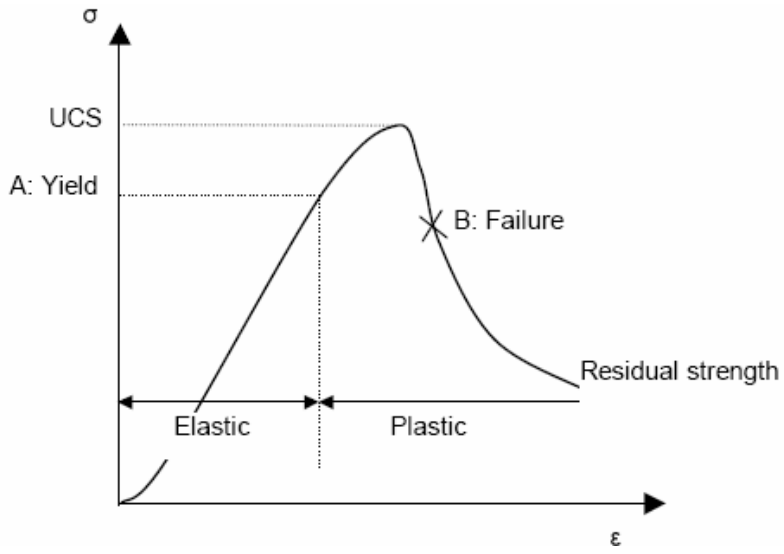

Figure 2-1: Sketch Map of Stress vs. Strain under Uniaxial Compression

(After Han, 2003)

Shear strength describes rock strength available to resist shear stress. The resistive forces include two parts: one is the cohesive resistive force caused by cementation and grain interlock arising from diagenetic processes (mineral cementation, other sources of cohesive bonding); the other is the frictional resistive force caused by contact (stress) between particles. The magnitude of frictional resistance depends on the internal friction angle, φ', of the material and the magnitude of the effective confining stress, σ'_n. The resistive force arising from the frictional strength is calculated as the product of σ'_n and $\tan(\varphi')$, which means that the resistance is proportional to the effective confining stress.

The residual strength is also illustrated in Figure 2-1. The residual strength refers to the strength that the rock has after losing its cohesive strength component. It is the lowest shearing resistance available after large shear deformations. Once a rock yields and damage continues to accumulate, the lowest shearing resistance is not only a function of the mineralogy, but is also related to the nature in which failure took place, the size and granulation of the fractured, damaged zone, the roughness of the shearing plane, etc. To a considerable degree, the ultimate strength of a rock depends on the stress path required to reach that condition, and is often related to the joints and discontinuities such as bedding planes (Dusseault 2005).

Tensile strength is the rock strength that prevents the solid matrix from being pulled apart by fluid flow or other driving forces that can lead to a tensile stress. Specifically, the tensile strength of a material is the maximum amount of tensile stress that it can be subjected to before rupture. The definition of rupture (tensile failure) can vary according to material type and design methodology.

Various methods are available for measuring rock strength. Strength can be determined by both static (or experimental) methods and dynamic (or logging-derived correlation) methods. Usually both lab and well log data are incorporated if possible, considering that none of the methods are intrinsically superior to the others. Triaxial testing of high-quality core samples in the laboratory is perhaps the most reliable approach in spite of its time-consuming nature and high cost. However, the samples provided for specimen preparation are always damaged to some unknown amount by stress relief. Well logs can be used to

reveal the *in situ* stress conditions and provide continuous curves of the strength trends of the formation. Unfortunately, no logging tools can directly yield static strength values. Dynamic methods based on sonic logging have difficulties related to how to interpret and calibrate logs appropriately in order to give a good estimate of the desired strength measure.

Moreover, rock strength is not a constant: it is affected by numerous internal factors such as grain size, mineral cement type, contact fabric, original cracks and fissures, anisotropy, etc., as well as external conditions such as water saturation, stress state, loading path and so on. This leads to great difficulties in obtaining accurate rock strength data, especially under *in situ* conditions hundreds of metres deep.

2.4 Rock failure theory

There are two major types of rock failure: shear failure and tensile failure. In shear failure, most of the weak mineral bonds between particles are destroyed by strain. Tensile failure results in particles being plucked out of the rock skeleton at the low- or no-cohesion stage. In a uniaxial material test, the length decreases in the compressive stress direction; the other two (unconfined) directions will increase in size. Tensile stress is the opposite of compressive stress and the rock tensile strength is the limit state of stress when the rock fractures. It is a measure of the force required to pull the rock apart. Large area casing failure is always related to the shear failure of rocks, and tensile rock failure is not considered important in this context.

Rock failure and rock yield are somewhat different concepts. For stability analysis, the accumulation of shear bands is a process of yield, but cannot be termed as failure until rock breaks or collapses and the loading stresses have shifted to the local vicinity of the induced shear plane. In Figure 2.1, the left part of the curve before point A is elastic deformation; the rock will recover to its original state after the loading stress is removed. After point A, rock undergoes plastic deformation and yields. Point B is the failure point, where the structure loses its designed functionality; this is not necessarily synonymous with the yield point.

The Mohr-Coulomb failure criterion (M-C criterion) is the most popular criteria among numerous empirical criteria to describe the onset of rock failure, it clearly captures and describes both frictional and cohesive strength factors in shear failure, it is easy to apply, and is relatively reliable:

$$|\tau| = c' + \mu' \sigma'_n \qquad (2.2)$$

Here, c' is cohesive shear strength, μ' is the effective stress friction coefficient, and σ'_n is normal effective stress. All parameters are considered to be effective stress parameters, as it is the effective stress that controls the strength.

Griffith demonstrated the importance of internal microscopic flaws that act as stress concentrators in controlling the strength of brittle materials (Griffith *et al.* 1920). Using this approach, fracture mechanics has been highly successful in relating defect structures to fracture strength and related properties, but fracture mechanics are generally not applied to casing shear problems.

2.5 Casing Failure Theory

Casing deformation is a geological engineering issue with complex mechanisms and multiple causal factors that include drilling and well completions, lithostratigraphy, and injection and production strategies. There are generally three typical forms of casing shear (Dusseault *et al.* 2001):

a. Localized horizontal shear at weak lithological interfaces within the overburden during reservoir compaction or heave.

b. Localized horizontal shear at the top of a specific production or injection interval caused by volume changes in the interval that arise from pressure and temperature changes.

c. Casing buckling and shear within the producing interval, primarily along perforations, and mainly because of axial buckling when lateral constraint is removed, but occasionally due to shearing at an intra-formational lithological interface.

It is also observed that the overburden shear failures are in general associated with large-scale formation movements (Silva *et al.* 1990).

2.5.1 Formation Shear and Slip Criterion

Inhomogeneities in strength and stiffness in specimens with cohesion result in the formation of a shear band, usually along a lithological interface (high stiffness contrast, therefore a high shear stress contrast) with a weak shale (low strength). In general, rather than general shear straining, one would expect shear distortion in such media to coalesce on a single interface, an observation confirmed in fields in Alberta, California, the North Sea and elsewhere (Silva *et al.* 1990).

The natural shear stresses, τ, exert a pre-existing thrust to the rock mass along the failure plane; when the thrust exceeds the slip criterion, slip is evidenced, but as long as it does not, the casing remains largely undeformed. Whether the casing is distressed or not depends on the magnitude of the shear slip along the critical weak surface. Furthermore, if the shale is pre-sheared by natural processes, evidenced as slickensides and bedding plane separation, the critical surface may be at a condition close to the minimum strength (called the residual strength in soil mechanics).

The maximum shear resistance of shale is also assumed to follow the Mohr-Coulomb law (Figure 2-2)

$$\tau_{\max} = c' + \sigma'_n \, tg\varphi' \qquad (2.3)$$

where $\tau_{\max}$ is the maximum rock shear resistance (MPa), c' is the cohesion (MPa), φ' is the angle of friction (°), and σ'_n is the effective normal stress (MPa).

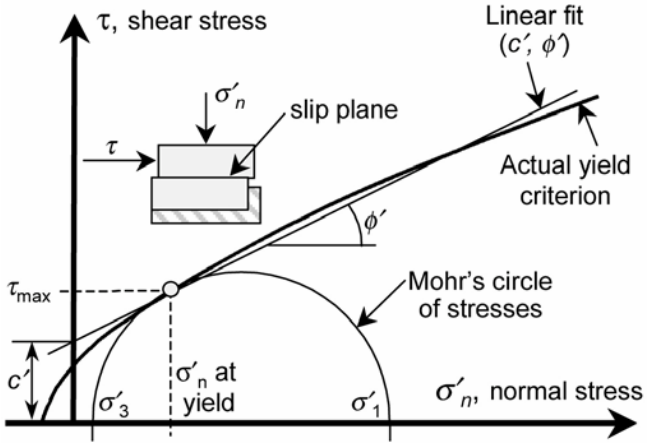

Figure 2-2: Mohr-Coulomb Criterion and Stress

2.5.2 Water Content Influence

Water content in the shale formation has an influence on shear resistance. In sub-surface conditions, a high pore pressure and the presence of available water can soften the shale through swelling (water uptake). The higher pore fluid pressures also mean lower effective stresses (refer to Equation 2.4).

$$\sigma'_n = \sigma_n - p_f \qquad (2.4)$$

where p_f is pore pressure (MPa).

In addition, because the shale is of low permeability, an elevated pore pressure will occur first along the interface with the more permeable sandstone or siltstone, adding another mechanism for localization of the shear deformation along the lithological interface.

Thus, prolonged high-pressure injection not only causes normal stress decrease and a lowered maximum shear resistance, an increase in the water content of the shale will also lead to a diminution (degradation) of cohesion, perhaps even a reduced friction angle in the critical shale-sandstone interface where shear stresses tend to be concentrated. Triaxial testing of shale specimens from the critically sheared region of one of the wells in Daqing

Oilfield verified an approximate relationship between the shale seam cohesion, friction angle, and water content (f_w):

$$c' = 96 - 5 \times f_w \qquad (2.5)$$

$$\varphi' = 34 - 2.7 \times f_w \qquad (2.6)$$

Under normal circumstance, the shale contains only 3 – 5% water, whereas, as the result of the prolonged high pressure water injection, shale was observed to develop higher water contents. In one of the damaged wells, the shale water content was measured at ~10%. Supposing that this occurred from swelling, if the relationships stated above apply, using the MC criterion, the maximum shear resistance of the shale will decrease by $0.378 \cdot \sigma'_n$ MPa. Furthermore, the area affected by such a strength reduction will grow with time as the pore pressures diffuse into the shale at an increasingly regional scale. This weakening effect is "additive" to the pore pressure effect, and when a sufficiently large area has been affected, the shale strength is overcome, making it possible for shear displacement to take place over a large area, akin to a thrust fault plane. Given the difficulty in precise assessments of conditions and material properties *in situ*, it is hard to unequivocally prove that the weakening effect is substantial, but the gradual development of shear distortion along planes is considered to be partly the result of water weakening, and partly the result of scale. Only when the scale length of the affected area exceeds a critical size can sufficient shear stress be developed to cause shear plane development.

2.6 Casing Stability Associated with Injection and Production Activities

Casing stability is closely associated with oil production activities such as drilling, producing, injecting, and well stimulation (e.g. perforating or hydraulic fracturing). Petroleum recovery activities induce changes in stress and pressure. Variation in stress and pressure may cause rock shear. Rock shear, in turn, causes casing shear. Dusseault *et al.* (2001) discussed in detail the casing shear issue associated with typical petroleum recovery activities such as

depletion, injection, and heating. In this section, I will briefly review compaction-induced shearing and injection-induced shearing, following his analysis.

2.6.1 Compaction-Induced Shearing

In the production of underground fluids without large amounts of injection, the process leads to an increase in effective stresses and a decrease in reservoir volume. The volume diminution of the reservoir induced by a reduction in porosity is termed compaction, which is usually associated with depletion. Compaction is a downward and inward motion due to the continuity of overlying rocks and the general lenticular cross-sectional shape of a reservoir.

The process corresponds to path A-B in Figure 2-3, which shows an experimental compaction curve for a stratum in a high porosity reservoir. Under conditions of pressure draw down Δp (path A-B), a porosity reduction of about 5% is evidenced.

When the compressibility of the reservoir is substantial, the strains may be large enough to induce casing shear. This may lead to the reactions in the overburden illustrated in Figure 2-4. The middle section experiences an increase in σ_h; while the remote flanks experience a drop in σ_h, and the rocks above the shoulders experience an increase in the shear stress. Whenever the shear stress in the overburden exceeds the rock strength of the bedding planes, low-angle slip will occur. The highest shear stress is generally on the shoulders of the structure. Vertically, the overburden shear stress is most intense near the reservoir (at the bottom of the overburden, often on a soft layer very near the reservoir).

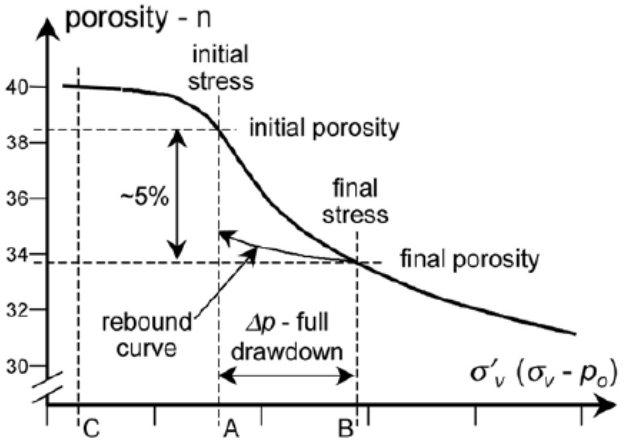

Figure 2-3: Reservoir Compaction Curve Showing Porosity Variation with σ'_v

(After Dusseault *et al.* 2001)

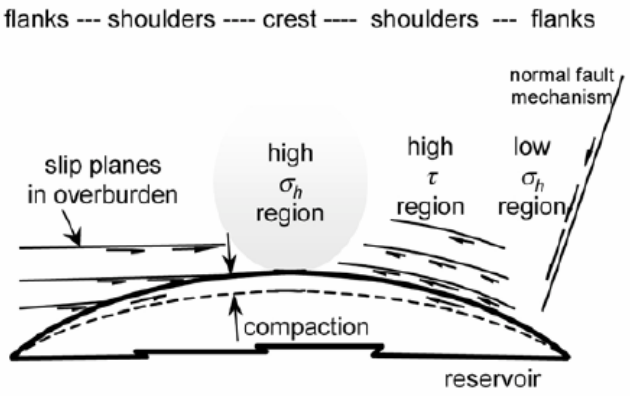

Figure 2-4: Compacting Reservoir Bedding Plane

(After Dusseault 2001)

2.6.2 Injection-Induced Shearing

Fluid injection into reservoirs increases pore pressure and decreases effective normal stress. As a result, the rocks in the reservoir are made easier to shear. Furthermore, reservoir expansion leads to shearing near bounding interfaces where stresses are concentrated.

The phenomenon of effective stress reduction and volumetric expansion due to high-pressure injection is also illustrated in Figure 2-3. Path A-C in Figure 2-3 corresponds to the process of injection.

Because bounding strata are impermeable seal rocks, they do not expand the same amount as permeable reservoirs. Therefore, in a reservoir subjected to high-pressure injection, a large shear stress is imposed on the interface between the reservoir and the bounding strata. Whenever the shear stress exceeds the rock strength, that is, the interface strength, slip will occur.

Figure 2-5 gives the general description of injection-induced shearing. The injection well can be a single well or a set of regular lines of injectors; the latter case is more critical for shear slip.

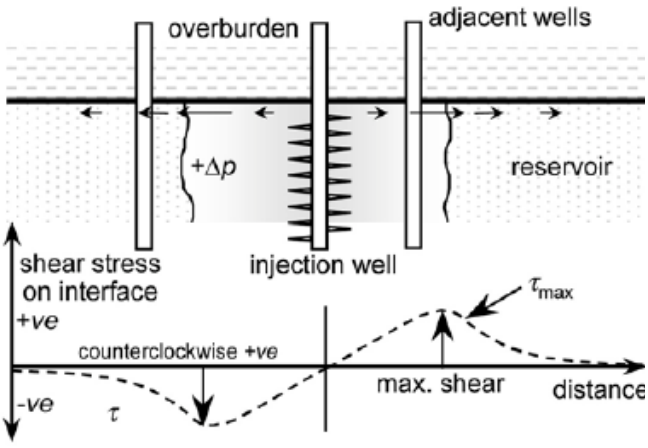

Figure 2-5: Injection Induced Shearing

(After Dusseault *et al.* 2001)

2.7 Summary

In most petroleum engineering problems, it is assumed that there are three principal stresses in the ground and one is vertical, σ_v, with the other two horizontal, σ_H and σ_h. From the magnitude point of view, there are major - σ_1 - intermediate -σ_2 - and minor - σ_3 - stresses.

As for which one is major and which one is minor, it depends on the actual stress field. The effective stresses are the differences between total stresses in the rock skeleton and the pore pressure in the interconnected voids.

There are mainly four forms of rock mechanical strength used: uniaxial compressive strength (UCS), shear strength, tensile strength, and residual strength. Rock strength is not a constant: it is affected by numerous internal factors, such as grain size, mineral cement type, contact fabric, original cracks and fissures, anisotropy.

Water saturation is an external condition that influences rock strength. Increased water saturation affects rock strength by decreasing both rock cohesion and rock friction angle. Water content in the shale formation has an influence on rock shear resistance. In subsurface conditions, higher water contents are correlated with higher pore pressures. Higher pressures mean lower effective stresses ($\sigma'_n = \sigma_n - p_f$). Therefore, high-pressure injection causes normal stress decrease and in turn lowers the maximum shear resistance. Also, higher water content in shale decreases cohesion and friction angle of the shale formation. In Daqing Oilfield, a 5% increase of water content in shale can decrease the maximum shear resistance of shale by approximately 40% of the normal stress.

Two types of rock failure arise from exceeding of rock strength by effective stresses. They are shear failure and tensile failure; the former is the most important to casing shear.

Large area casing failure is always related with shear failure of rocks. Petroleum recovery activities can induce casing shear. There are generally three typical forms of casing shear: horizontal shear at weak lithological interfaces within the overburden; horizontal shear at the top of a specific production or injection interval; and casing buckling and shear within the producing interval.

Chapter 3
Reservoir Heterogeneity and the Effects of Pressure Changes

3.1 Introduction

Reservoir heterogeneity is important to the understanding and effective production of oil and gas reservoirs. Reservoirs can contain impermeable or low-permeability lithological units as well as highly permeable reservoir rocks, which in turn may possess heterogeneous porosity and permeability distributions. Heterogeneity also exists in all other intrinsic properties of the rocks, including rock mechanics properties. These reservoir heterogeneities can further be affected by complex fault systems that influence fluid flow paths and distribution. Reservoir heterogeneity occurs at all scales from the individual grain to scales approaching that of the reservoir itself.

Many methods are available for studying the physical properties of heterogeneous porous media. Laboratory experimental approaches exist for characterizing heterogeneity, and these methods have more recently focused on numerical simulation methods.

Alpay (1972) put forward a method for determining reservoir heterogeneity. Instead of involving detailed mathematical heterogeneity descriptions in routine applications, something requiring specific detailed information that is not easily available, his method relied on the investigation of the sedimentary stratigraphic makeup of reservoir rock to describe physical and textural variations in the reservoir. He broke down reservoir heterogeneity into three classes according to various reservoir anatomical component scales. The classes are: microscopic heterogeneity, macroscopic heterogeneity, and megascopic heterogeneity. Each class has its own characteristics. Reservoir heterogeneity can be determined by characterizing the items in his three classes of heterogeneities.

In Daqing Oilfield, lithostratigraphy, structural styles, and facies architecture are the three fundamental elements that define the reservoir heterogeneity, and eventually influence or determine the development regime. Many research articles (Wang *et al.* 1995, Liu and Wan 1995, Guo *et al.* 2000, Lu *et al.* 2000, Yan *et al.* 2005, Liu *et al.* 2006) have been devoted to heterogeneity analysis in the field of reservoir development, with impacts on infill well deployment, technical measures such as polymer choice and workover method, and production profile control (controlling the rates of injection and production from individual beds in a series penetrated by a single well).

No articles have been found in the general literature concerning casing shear analysis from a reservoir heterogeneity point of view. In this chapter, reservoir mega-heterogeneity, reservoir macro-heterogeneity, reservoir micro-heterogeneity, and the effects of pressure change will be discussed. In a later chapter (Chapter 5), simulation of casing shear in a heterogeneous reservoir will be described.

3.2 Megascopic Heterogeneity

The megascopic heterogeneity can be described from the structural geometry, faults, and folding points of view (Alpay 1972), larger than the scale of individual beds or units. Daqing Oilfield has a generally simple geometry, i.e., a relatively flat structure. Although there are a large number of faults, the areal distribution of faults (intensity and magnitude) seems to be similar for the overall oilfield. No obvious large scale folding is found, and there are also no obvious large-scale fracture systems or fractured regions at the megascopic scale.

Daqing Oilfield is in the middle of the depression of the Songliao Basin on a secondary structure belt. The structure of the oilfield is an elongated flat anticline with a surface area of around 11,000 km^2. The strike of the anticline is nearly in the North-South direction, and the dip angle of the fold strike is around 1º-2º. The western limb dip angle of the anticline is 4º-6º, whereas the eastern limb dip angle is only 1º-2º (Chen *et al*. 2002). Among the seven identified areas that have shown the most serious shearing, five of them are on the fold crestal area (hinge area), and two of them are on the limb (shoulder or flank) of the anticline.

However, the division of these areas in this manner is not very clear because of the very flat structure.

During the geological history of the basin's evolution, it first underwent nearly East–West extensional stressing, followed by the imposition of a nearly E-W direction compressive stress in Cenozoic time. (Details will be discussed in Chapter 5.) Most faults in Daqing Oilfield are normal faults with ~NW-SE azimuth (refer to Figure 5-1). Because of the changing of stress field in geological time ("pull" followed by "push"), most faults in the oilfield have established a "chair" shape (Figure 5.4). Neither thrust faults nor folding are found, but formation shapes near faults are changed due to the "Pull-Push" events. Local increase in thickness of formations near faults can be observed. No areal concentrations of casing shear were observed along fault planes because drilling was usually designed to avoid faults in order not to lose too much productive interval thickness.

Therefore, it may be concluded that the megascopic heterogeneity of the Daqing Oilfield is not severe, compared with its macroscopic and microscopic heterogeneity. The geometry is simple, the structure is flat, faults are numerous but distributed evenly, and no large-scale folds and fractures are found. There is no obvious relationship between megascopic heterogeneity and large area casing shear. When considering the concentration of casing shear in the shale formation above the injection and production intervals, a relationship with macro- and/or micro-heterogeneity is suggested.

3.3 Macroscopic Heterogeneity

Daqing Oilfield is in a continental fluvial-delta sedimentary environment with complex geological conditions and large contrasts in permeability. Reservoirs are encountered at depths of 700 to 1200 m; many different oil-bearing zones exist, and there is a high degree of heterogeneity both horizontally and vertically. Heterogeneity is linked to evolution of reservoir facies under varied depositional environments, structural styles present at the time of deposition and changes imposed by post-depositional tectonic and diagenetic activities. These are instrumental in imparting vertical-lateral heterogeneity within the reservoir.

The heterogeneous multi-layer continental sandstone reservoirs in Daqing Oilfield have various different depositional facies horizontally. The depositional facies can be subdivided into micro-facies such as channel facies, delta inner front facies, and delta outer front facies. Sand body geometries, distribution dimension and physical properties among the facies vary greatly. The lowest air permeability of the reservoir is one mD (one milliDarcy), while the highest is more than 5000 mD (Lu *et al.* 2000). Moreover, the facies are alternating and separated by mudstones or shales. There are still some unexploited very low and ultra-low permeability siltstone reservoir zones in which oil is found but whose geologic reserves are not calculated (called "untabulated reservoir" - Liu *et al.* 1995). The following figure (Figure 3-1) generally describes the horizontal heterogeneity of the central area in Daqing Oilfield. The black colour indicates channel facies area, the gray colour indicates interfluvial facies, while the white areas are shale or mudstone areas.

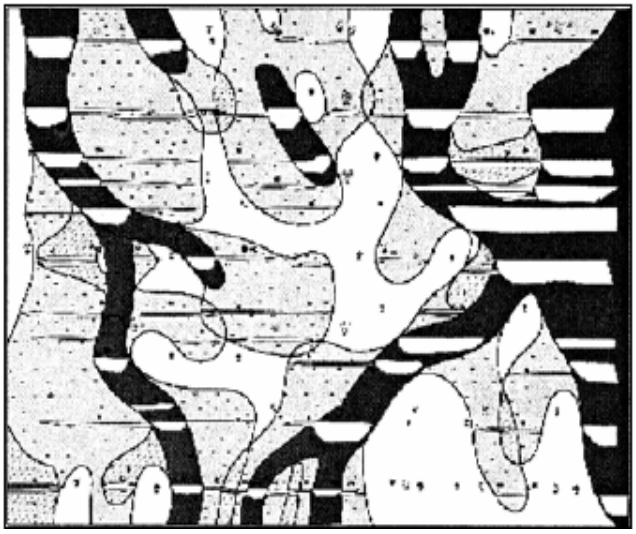

Figure 3-1: Depositional Facies Map

The black colour areas are channel facies area, the white colour inside black areas indicates thickness of sand bodies. The gray color areas are interfluvial facies areas that have low permeability and poor physical properties. The white colour areas are mudstones and shale areas. Small dots indicate well positions. (After Yan *et al.* 2005)

Vertically, oil zones in Daqing Oilfield are part of a Lower Cretaceous, fluvio-deltaic sedimentary sequence that contains up to 100 individual sand layers with thickness ranging from 0.2 meters to 20 meters (Osmar *et al.* 1990). These layers are mainly sandstone or siltstone with a porosity range from 20% to 30% (average 25%) and a permeability range from 20 to 1600 mD (average 230 mD). According to sedimentary unit division criteria developed in recent years, the layers can be further subdivided into 120~150 single sand layers with thickness of 1~3 m (Lu *et al.* 2000). Furthermore, there are a number of stacked sand-silt-shale sequences, and a thick overburden shale layer (~60 m). Figure 3-2 gives a general description of the sand-silt-shale sequences with the thick shale layer of the upper overburden rocks. Figure 3-3 is the real vertical profile of the reservoir in the central area. The figure reveals both the vertical heterogeneity and horizontal heterogeneity. Different shading styles identify sands of different facies types.

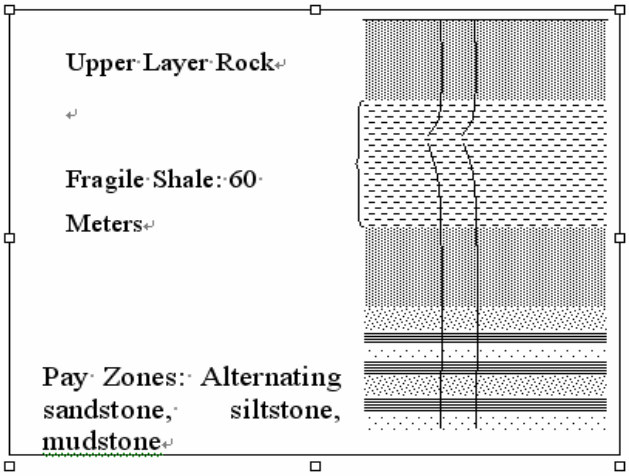

Figure 3-2: Sketch of Reservoir Sequence

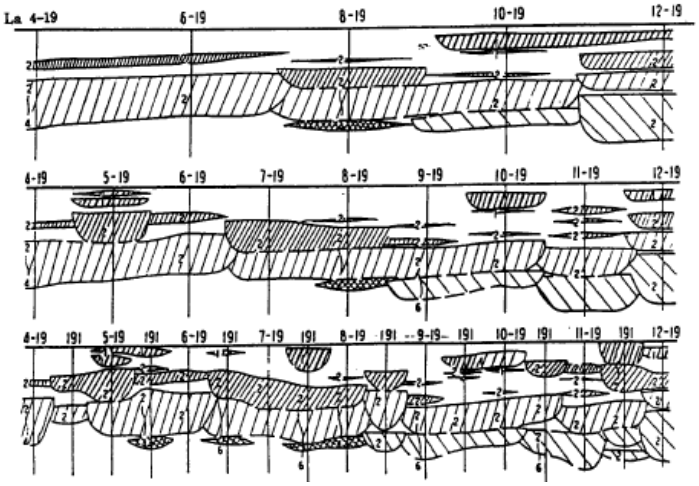

Figure 3-3: Vertical Profile of Reservoir Sand Bodies

(After Liu *et al.* 1995)

Great property differences in inter-layer and inner layer conditions caused great differences in recovery rate after long periods of water flooding. Certain thin reservoirs have not been watered-out, others have been. Pilot tests of commercial development of such *"untabulated resevoirs"* shows that isolated untabulated reservoir units have some productivity after hydraulic fracturing (Liu *et al.* 1995). Also, there exists a considerable amount of residual oil both in areal distribution and in individual layers due to differential sweeping by the injected water in large and medium-scale channel sand bodies. Figure 3-4 shows areas of potential residual oil area marked by shading. Vertically, analysis of cored wells shows that the watered-out thickness of thick sand bodies is near 80%, but the water displacing oil efficiency inside layers is less than 40%, while 20-30% of the strata are not watered-out, representing potential additional resources.

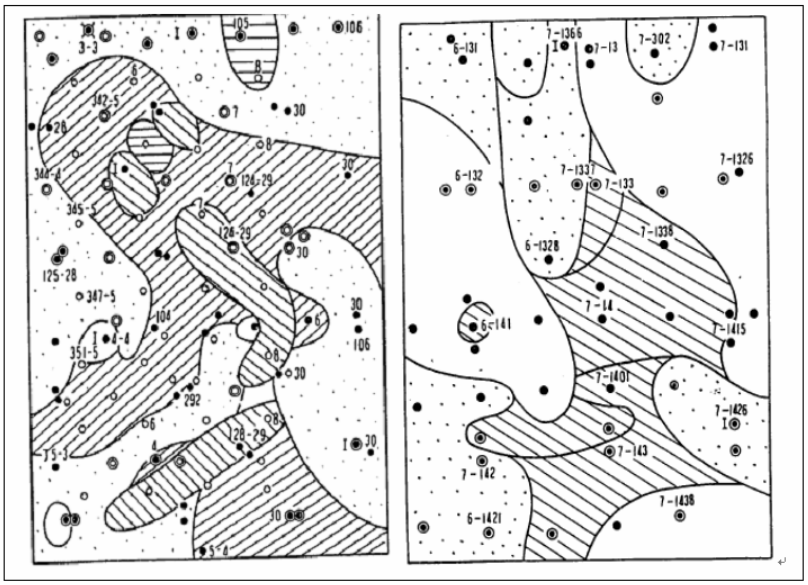

Figure 3-4: Maps of Potential Residual Oil Area

(After Liu *et al.* 1995)

3.4 Microscopic Heterogeneity

Reservoir macro-heterogeneity generally is not too difficult to understand, to characterize, and to take measures to handle it during production operations. Taking Daqing Oilfield as an example, the oilfield was not thought to have a serious heterogeneity problem until a rapidly rising water-cut was observed after only a short period of production. After that, separate layer injection, separate layer production, and controlled infill drilling were used to cope with the influence of heterogeneity. However, micro-level heterogeneities, such as pore throat size distribution, pore structure, and anisotropy, are not very easy to identify quantitatively. Some efforts have been made to identify pore-scale heterogeneity of some reservoirs in Daqing Oilfield (Shen *et al.* 1995, Han *et al.* 2000, Peng *et al.* 2002, Han *et al.* 2006). These efforts include pore structure characterization, fractal dimension assessment, and micro-scale anisotropy analysis.

3.4.1 Pore Structure Characterization

Many methods of pore size distributions measurement are available. They are mainly mercury porosimetry methods, photo-micro-graphic analysis methods, and sorption-desorption methods. Considering the heterogeneous properties of pore sizes of reservoir zones in Daqing Oilfield, one finds a wide length range from several nanometers to thousands of micro-meters. However, no single experimental technique can yet provide a quantitative description of rock micro-architecture over length scales spanning four to five orders of magnitude. Direct imaging methods (Ruzyla 1984) cannot provide statistically significant micro-structure data at length scales smaller than 1 micro-meter. Indirect imaging methods, such as small-angle neutron scattering (SANS/USANS) or small-angle X-ray scattering (SAXS), reveal pores ranging from one nanometer to about 10 micro-meters (Radlinski *et al*., 2002). Nuclear magnetic resonance (NMR) relaxation methods (Shen 1992) can only semiquantitatively provide characteristics of pore sizes and results of such analysis can be distorted by diffusional averaging of magnetization between pores (Chang and Ioannidis 2002). The mercury intrusion porosimetry (MIP) method may be used to probe the distribution of pore volume in the range 20 nm to 100 μm; unfortunately, the method provides only the distribution of pore volume accessible to mercury through pore throats of different size.

Combinations of mercury porosimetry and photo-micro-graphic analysis can lead to a better understanding of pore accessibility and pore structure characterization in general (Dullien 1979). Radlinski *et al*. (2002) presented a method of determining the pore size distribution based on the statistical fusion of small-angle neutron scattering (SANS) and backscatter SEM (BSEM) data by utilizing surface fractal properties of rocks (Radlinski *et al*. 1999). The results have provided the pore size distribution in the range 1nm to 1mm. Amirtharaj *et al*. (2003) presented a MIP and BSEM combined method using information obtained from MIP instead of SANS. To identify pore size distribution of cores from Daqing Oilfield, a similar method that combines mercury intrusion porosimetry (MIP) and backscatter SEM (BSEM) data was used.

From a statistical point of view, supposing it is homogeneous, a porous medium may be generally described in terms of a binary phase function Z(x), taking the value of unity if the x point is in the void phase, and zero otherwise (Ioannidis *et al*. 1997). The moments of the phase function Z(x) are the porosity and the two-point correlation function:

$$\phi = \langle Z(\mathbf{x}) \rangle \tag{3.1}$$

$$S_2(\mathrm{r}) = \langle Z(\mathrm{x}) Z(\mathrm{x} + \mathrm{r}) \rangle \tag{3.2}$$

where r is a lag vector and angular brackets denote statistical averages. The two-point correlation function $S_2(r)$ depends only on the modulus of the lag vector for isotropic media. By analyzing binary photographs of pore samples, the correlation function $S_2(r)$ can be determined.

The above two-point correlation function can be used to calculate the autocorrelation function (Equation 3.5). The integral scale of the autocorrelation (Equation 3.4), together with the average image porosity, can be used to correlate permeability values, as described in Equation 3.3 (Ioannidis *et al.* 1996):

$$\log_e(k) = a + b\log_e(\phi) + c\log_e(I_s) \tag{3.3}$$

$$I_s = \int_0^\infty R_z(r)dr \tag{3.4}$$

$$R_z(r) = (S_2(r) - \phi^2)/(\phi - \phi^2) \tag{3.5}$$

In the above equations, $S_2(r)$ is the two-point correlation function; $R_z(r)$ is the autocorrelation function; I_s is the integral scale of autocorrelation function; k is permeability; and, a, b, and c are coefficients and can be determined by linear regression.

In small-angle scattering (SAS) experiments, the measured scattering intensity $I(Q)$ can be calculated through the equation (Radlinski *et al*. 2002):

$$I(Q) = \frac{d\sigma}{d\Omega}(Q) = 4\pi \int_0^\infty r^2 \gamma(r) \frac{\sin(Qr)}{Qr} dr \tag{3.6}$$

Here $\gamma(r) = (\Delta\rho)^2 \cdot \phi(1 - \phi) \cdot R_z(r)$, $(\Delta\rho)^2$ is the scattering length density contrast, a material

constant depending on grain density and chemical composition, and Q is the magnitude of the scattering vector. For periodic structures, the magnitude of the scattering vector is related to the characteristic size of the scattering object by $Q = 2\pi \cdot r$ (Radlinski *et al.* 1999). If $S_2(r)$ is experimentally available from BSEM images over a range of **r** values, $I(Q)$ can be calculated in the corresponding Q-range using equation (3.6).

Fractal analysis of MIP data is based on the following scaling law:

$$-dS_{Hg}/dr \propto r^{2-D} \qquad (3.7)$$

where $S_{Hg}(r)$ is the sample saturation to mercury at capillary pressure $P_C \propto 1/r$. Equation (3.7) is consistent with a scaling of the number-based pore size distribution according to the power law $f(r) \propto r^{-(D+1)}$. Over a limited range of pore length scales, $I(Q)$ data computed from $S_2(r)$ via equation (3.6) also follow the scaling $I(Q) \propto Q^{D-6}$, thus providing an estimate of D that can be compared to the one obtained by analysis of MIP data using Equation (3.8). Provided that correspondence between the two values is established, one may extrapolate $I(Q)$ in the large Q-range according to $I(Q) \propto Q^{D-6}$. Thus, structural information about pore length scales not probed by BSEM may be accounted for quantitatively and consistently.

To obtain the complete distribution of pore length scales from the extended $I(Q)$ data, it is assumed that the solid-void interface has a locally spherical geometry. According to this assumption, the scattering intensity per unit volume is given by (Radlinski *et al*. 2002):

$$I(Q) = (\Delta\rho)^2 \frac{\phi}{\langle V_r \rangle} \int_{R_{\min}}^{R_{\max}} V_r^2 f(r) F_s(Qr) dr \qquad (3.8)$$

In Equation (3.8), R_{max} and R_{min} are the maximum and minimum pore radii, respectively, $Vr \equiv V(r) = 4/3\pi r^3$ is the volume of a sphere of radius r, $\langle V_r \rangle = \int_{R_{\min}}^{R_{\max}} V_r f(r) dr$ is the average pore volume, $f(r)$ is the probability density of the pore size distribution, and $F_s(Qr)$ is the form factor for a sphere of radius r given by:

$$F_s(Qr) = \left[3 \frac{\sin(Qr) - Qr\cos(Qr)}{(Qr)^3} \right]^2 \qquad (3.9)$$

The function *f(r)* is determined by inversion of the extended *I(Q)* data using Equation (3.8). The cumulative distribution of pore volume by *pore size* is then computed from *f(r)* and plotted along mercury porosimetry data as a function of the equivalent capillary pressure for purposes of comparison.

Samples used for the experiments were cut from a set of 11 core sections taken from Daqing Oilfield. Samples were washed by toluene before mercury porosimetry and image analysis. The calculated results based on experimental data, together with core and log measurements of porosity and permeability, are listed in Table 3-1. Porosity values obtained from image analysis were carefully compared with mercury porosimetry data and data provided by Daqing Oilfield personnel from log analyses to make sure of the effectiveness of the measurement method. The predicted permeability (Column 4 in Table 3.1) was calculated using Equation 3.3. The second column in Table 3.1 is measured air permeability for "as-is" (not cleaned) samples. A large difference was found between these two columns because of possible clay content influence in void spaces (the image analysis method is less sensitive to the presence of clay than the direct measurements). However, the result is similar to the result (Table 3-2) taken several years ago on clean core samples of another well through similar core image analysis method (Peng *et al.* 2002).

Table 3-1: Summary of Petrophysical and Image Analysis Measurements(A)

#	k_{core}[(1)] (mD)	k_{log}[(1)] (mD)	k_{pred} (mD)	ϕ[(1)]	ϕ_{img}	ϕ_{MIP}	D_{img}	D_{MIP}
1	4254	1180	2217	0.306	0.304	0.397	2.61	2.76
2	840	543	1336	0.322	0.329	0.274	2.51	2.51
3	6568	1189	2389	0.308	0.260	0.233	2.72	2.72
4	2823	1194	669	0.308	0.280	0.255	2.68	2.82
5	2823	1194	1634	0.308	0.306	0.280	2.6	2.72
6	454	855	1498	0.280	0.297	0.255	2.61	2.61
7						0.291		
8	56	152	696	0.303	0.20	0.187	2.9	3
9	1123	998	2036	0.31	0.361	0.245		
10	311	999	967	0.304	0.296	0.242	2.64	2.64
11					0.295	0.282		

[(1)] Data supplied by Daqing Oilfield Company, Daqing, PR China.

Table 3-2: Summary of Petrophysical and Image Analysis Measurements(B)

#	Porosity（%）			Permeability（mD）		
	Experiment Value	Calculated Value	Difference (%)	Experiment Value	Calculated Value	Difference (%)
a1	30.0	28.7	4.3	1766	1679	4.9
a2	26.9	27.8	3.3	1030	1431	38.9
a3	25.2	25.6	1.6	818	946	15.6
a4	28.1	29.0	3.2	591	566	4.2
a5	23.4	24.7	5.6	295	320	8.5
a6	22.0	20.8	5.5	91	101	11.0
a7	20.1	20.0	0.4	39	61	56.4

(After Peng *et al.* 2002)

Experimental values of porosity and air permeability for samples listed in Table 3.2 were taken under room temperature conditions and up to 5.5 MPa pressure. Calculated porosity values were obtained using methods similar to those reported by Ioannidis (1996), although calculated permeability was also obtained from image analysis, but in a different way. A 3-D cubic model was first simulated from images data using the Sequential Indicator Simulation method; then, fluid flow through the simulated porous media was simulated and permeability calculated thereafter (Peng *et al.* 2002).

In both cases, core samples revealed very similar porosity; their main difference lies in permeability, which varied between 10 and 1000 mD.

3.4.2 Complete pore size distributiom

The computation of *I(Q)* data from binary images and MIP data and the interpretation of these data to obtain the pore size distribution are illustrated in Figures 3.5, 3.6, and 3.7 using Sample 2 as an example. Figure 3-5 shows how the surface fractal dimension is calculated from MIP data using Equation (3.7). The analysis yields D = 2.51. The calculation reveals that the pore range accessible by mercury intrusion is 0.02 μm to 180μm.

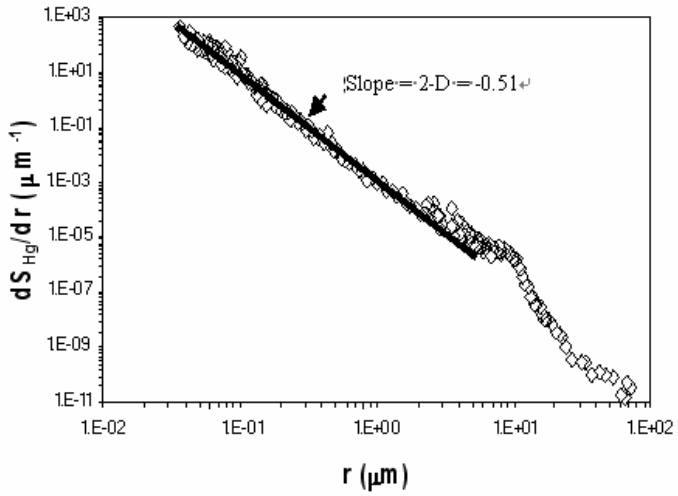

Figure 3-5: Determination of Surface Fractal Dimension (D) from MIP Data

Figure 3.6 shows the trend $I(Q) \propto Q^{D-6}$, with D = 2.51, of the *I(Q)* data computed via Equation (3.3) from the average image statistical properties.

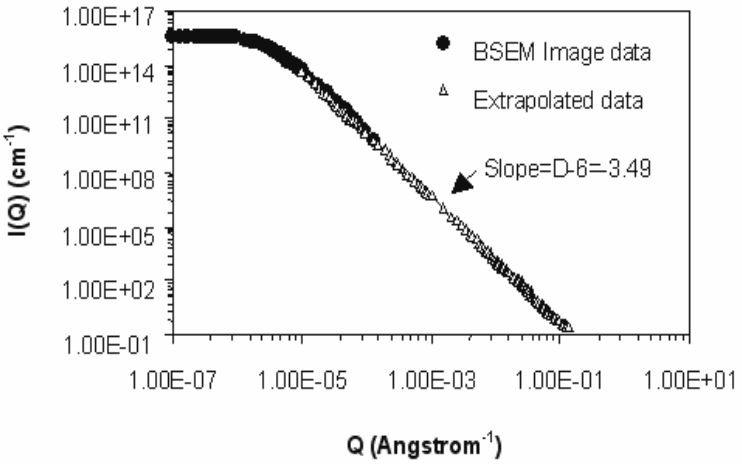

Figure 3-6: Determination of Surface Fractal Dimension by Extrapolation of BSEM Data and Fitting of I(Q) Data

The fitting of the extended *I(Q)* data by Equation (3.8) produces the pore size distribution $f(r)$ shown in Figure 3-7 using Sample 2 as an example. This distribution obeys $f(r) \propto r^{-(D+1)}$ with D = 2.51 in the pore size range of 0.01 to 1000μm.

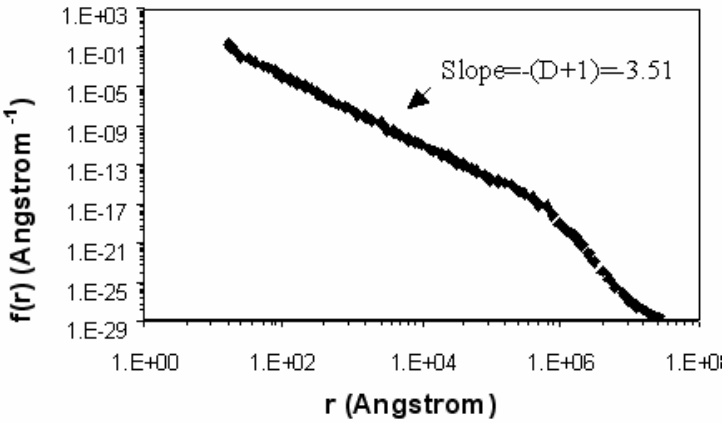

Figure 3-7: Complete Pore Size Distribution by Statistical Fusion of MIP and BSEM

3.4.3 Cumulative Pore Volume Distribution

Cumulative pore volume distributions calculated from *f(r)* are compared to the mercury porosimetry data for the samples. Taking Sample 2 as an example, Figure 3-8 gives cumulative pore volume distribution by pore size (PVD), accessible pore volume distribution by pore throat size (MIP), and simulated MIP result assuming complete pore accessibility and constant pore-to-throat aspect ratio of 3. From Figure 3-8, we notice that the pore volume distribution (PVD) spans five orders of magnitude of length scale.

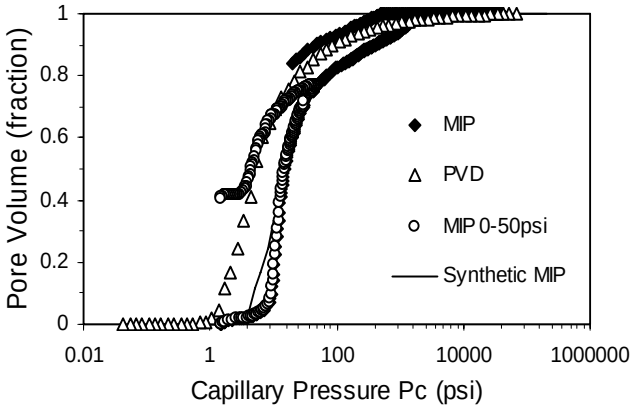

Figure 3-8: Cumulative Pore Volume Distribution

3.4.4 Pore-Throat Aspect Ratio

An apparent pore-to-throat size aspect ratio is defined as the ratio r_p/r_t. The value can be determined by a shift between the distribution of pore throat size (measured by the mercury intrusion curve) and the PVD. The aspect ratio for all samples in the experiment was 2 to 4 in value. Using the average pore-throat aspect ratio, we can create a synthetic MIP curve by a shift of PVD (as shown in Figure 3-8).

From the above pore structure analysis, these silty samples revealed similar porosity and mineralogy with a pore-throat aspect ratio range is 2-4 in value. Their main difference lies in permeability, which varied between 10 and 1000 mD.

3.4.5 Fractal Dimension Assessment

Fractal dimension has been used to quantitatively describe the heterogeneity of pore structure of sandstone in Daqing Oilfield (Shen *et al.* 1995). Fractal dimension of pore structure is calculated from the mercury-injection capillary pressure curve of the rock. It is believed that the larger the fractal dimension of pore structure, the more heterogeneous the pore structure for sandstones; sandstones with gravel and pinhole-porosity dolomite rocks would be considered most heterogeneous at the micro-scale. Fractal dimensions of core samples in Daqing Oilfield were found to be around 3.0 in both research programs (Shen *et al.* 1995 and Han 2006).

From Table 3.1, fractal dimension, D, was in the range of 2.51 to 3 (calculated from MIP), or in the range of 2.51 to 2.9 (estimated from image analysis). Sample 2 has the smallest fractal dimension, 2.51; Sample 8 has the largest, 3.0. Sample 8 is more heterogeneous than Sample 2. BSEM pictures appear to reflect this general assessment conclusion (Figure 3.9).

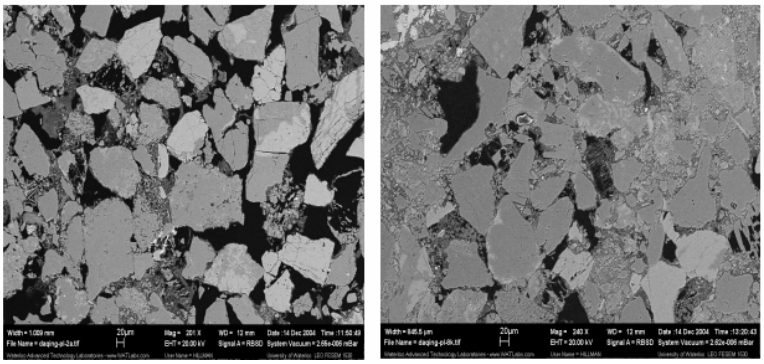

Figure 3-9: BSEM Pictures of Sample 2 (left) and Sample 8 (right)

3.4.6 Micro-scale Anisotropy

Although the above analysis of samples did not reveal much heterogeneity, there must be some micro-scale non-homogeneity, considering the large permeability difference. Further CT scan and compressional wave velocity measurements have been conducted in Stanford University on another set of samples to analyze micro-scale anisotropy (Han *et al.* 2000).

Figure 3.10 shows the textural variations revealed by CT-scans for one of the samples from Daqing Oilfield. Density variations are between 1.4 and 2.0 g/cm. The sample shows strong structure anisotropy.

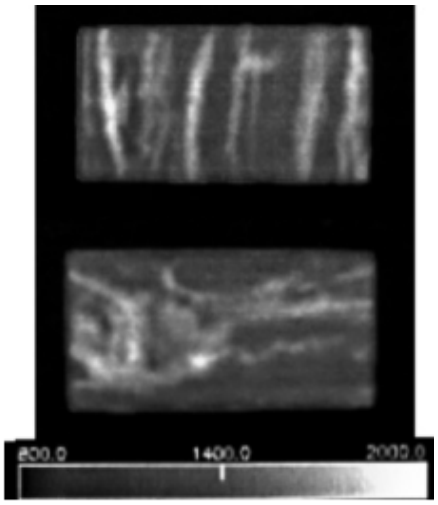

Figure 3-10: CT-scan of Sample (Vertical and Horizontal Direction)

Helium porosity, Klinkenberg-corrected air permeability, XRD mineralogy, and ultrasonic velocity were also measured for these sandstones from the Daqing Oilfield. All the samples were cleaned using toluene before measurements. XRD mineralogy analyses were carried out on powdered samples of the sandstones. Permeability anisotropy was calculated as the ratio of permeability difference between different directions to the average permeability of the samples. A summary of the XRD mineralogy, porosity, and permeability is given in Table 3-3. The samples have porosity range of 19 – 25% and permeability range of 0.1 – 1000 mD, and are very similar in mineralogy and in porosity. They are fairly clean sandstones consisting mainly of quartz and plagioclase with clay contents between 5 – 10%. Permeability anisotropy values ranged between 0 – 200%. The samples have similar mineralogy and porosity; the main difference lies in permeability and permeability anisotropy. The results of permeability and permeability anisotropy are consistent with the results of CT scans. This means that the different micro-structures are directly responsible for the great differences in permeability, as seems logical.

Table 3-3: Mineralogy, Porosity, and Permeability of All Samples

#	Mineralogy (%)					Permeability (mD)			Porosity (%)	
	Qua-rtz	Plagio-clase	Pota-ssium	Clay	Other	Hori-zontal	Verti-cal	Anis-otropy	Hori-zontal	Verti-cal
10	70	17	1	9	3	68	3.9	178%	23.9	25.2
11	41	25	25	5	4	295	41	151%	23.4	26.9
12	43	21	25	9	2	818	426	63%	25.2	29.2
15	61	25	2	10	2	7.6	7.6	0%	19.8	24.3
19	52	36	2	9	1	91	36	87%	22.4	25.6
21	63	22	2	10	3	1.4	0.21	148%	19.1	22.3
24	68	27	-	4	1	1030	677	41%	26.9	26.2
25	60	26	3	9	2	67	0.84	195%	20	18.8
26	54	29	4	11	2	39	45	14%	20.1	26.3
28	52	36	1	10	1	22	1.5	174%	23.2	23.6

Porosity values measured in horizontal and vertical directions are similar, whereas the permeability data differed considerably with direction. Permeability anisotropy ranged between 0 and 178%. These samples also had the largest permeability anisotropy among those tested.

Figure 3-11 shows the effect of stress on sonic velocity for samples. The samples show a general increase in velocity with stress. There is a difference in the rate of increase in velocity in horizontal and in vertical directions for the different samples. In some cases, a large velocity anisotropy at low stress decreases to near zero at 25 MPa. In other samples, velocity anisotropy remains high even at a stress of 25 MPa. In most samples, the rate of change of V_P with stress is greater at low stresses (up to 15 MPa); at high stresses, V_P changes only slightly. The different behavior of V_P gives an indication of the type of pores in the samples. From Griffith theory, a steep increase in V_P at low stresses is indicative of the closing of micro-cracks or pores with large aspect ratios (i.e. flat voids).

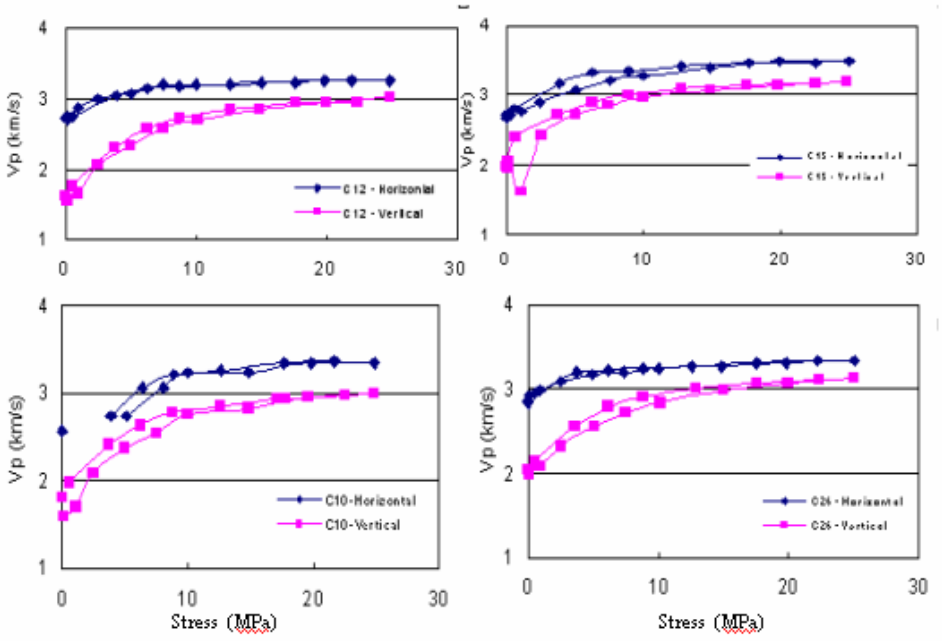

Figure 3-11: Velocity Variations with Stress in both Horizontal and Vertical Directions

The samples have similar porosity and mineralogy; their main difference lies in permeability, which varied between 10 and 1000 mD. Pore space interconnectivity is an important factor governing seismic wave propagation characteristics, and micro-structural variations also affect attenuation of ultrasonic waves.

Mineralogy measurements, ultrasonic measurements, and CT-scan results indicated that sandstones in Daqing Oilfield mainly contain quartz and plagioclase with uneven clay contents in the pore spaces. Layering of materials of different acoustic impedance and unevenly aligned grains and cracks lead to the large permeability range and great permeability anisotropy. These micro-heterogeneity factors cause pore parameters to behave unevenly (differently) under stress variations.

3.5 Pore Parameter Changes under Pressure

As stated in the above section, compressional wave velocity increases with the increase of effective overburden stress, which is also an indication of permeability decrease. Actually, porosity and permeability of porous and fractured geological media decrease with the exploitation of formation fluids such as petroleum and natural gas. For a depleting hydrocarbon reservoir, the decrease in pore pressure as a result of production can have a significant impact on the physical properties of the formation. Deformations commonly observed in producing reservoirs include compaction, fault reactivations and surface subsidence. Understanding the deformation mechanisms associated with these changes has important implications for many aspects of oilfield development from exploitation schemes to environmental management. Both fluid withdrawal and fluid injection appear to have induced active faulting (Chan 2004). A better knowledge of physical properties of formations and how they will be affected by the exploitation scheme is needed to minimize the damage associated with production. Many have reported calculation methods and models to analyze reservoir compaction, surface subsidence, and casing damage (e.g. Fredrich 1998 and 2000, Ibekwe 2003). Extensive laboratory study on the influences of pressure change to permeability and pore parameters have also been made (Chen *et al.* 2002, Chan *et al.* 2004).

Chen *et al.* (2002) establishes a method which allows for the measurement of permeability, porosity, and pore size distribution of cores simultaneously by using low-field nuclear magnetic resonance (NMR) relaxation time spectrometry. The method was applied to three siltstone samples from Daqing Oilfield. The samples were cored with their axis approximately parallel to the bedding planes of the formation. The coring processes were carefully monitored and cores selected and prepared to avoid as much as possible any extraneous influences on core properties, especially anything that would affect or alter the micro-fracture system characteristics. The cores had a diameter of 3.8 cm and a length of 7.6 cm. Core 20 had a natural fracture along the axial direction of the core extending over its whole length, Core 39 had a fracture along the axial direction of the core extending over half the length, and Core 52 was an intact matrix core without macroscopically visible fractures. The average clay content of the samples is 10.3% (a little bit higher than those used for CT-scan and ultrasonic velocity measurement); the relative content of clay is about 50 to 60% illite, 20 to 30% chlorite, and 26% illite–smectite mixed-layers minerals. Cores were cleaned with ethanol and benzene by an oil extraction method. Cores were saturated with kerosene under vacuum conditions to minimize the interaction with the rock minerals that might occur if water were used (Chen *et al.* 2002).

Figures 3-12 through 3-14 show the change of porosity ϕ relative to the initial porosity ϕ_0 with varying effective overburden stress σ' for all three cores. As stated in Chapter 2, the effective overburden stress is the difference between overburden stress and fluid pressure at the inlet. The decrease of formation pressure is simulated by increasing the effective overburden stress. The recovery procedure is simulated by decreasing the effective overburden stress.

Decrease of relative porosity with increasing effective overburden stress (corresponding to the decrease of formation pressure) and recovery of porosity with decreasing effective overburden stress (corresponding to the increase of formation pressure) are shown for all three cores. Hysteretic behavior shows an unloading recovery of 95% or so for core 20 and Core 39.

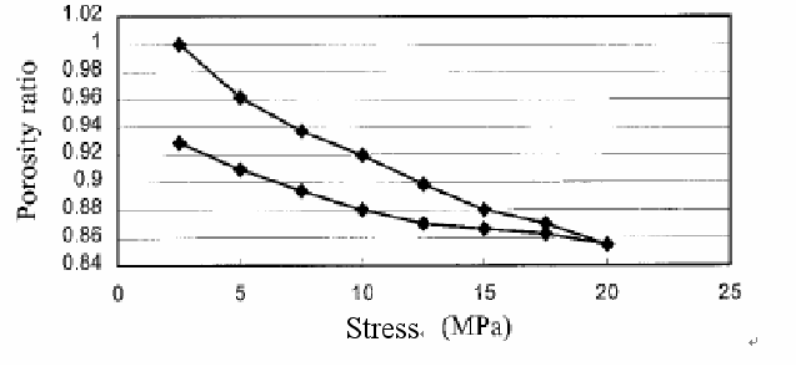

Figure 3-12: Relationship of Porosity Ratio and Effective Overburden Stress for Core 20

(After Chen *et al.* 2002)

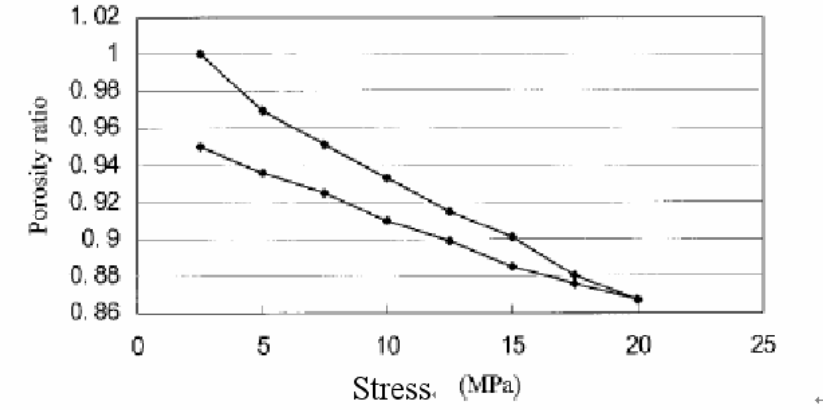

Figure 3-13: Relationship of Porosity Ratio and Effective Overburden Stress for Core 39

(After Chen *et al.* 2002)

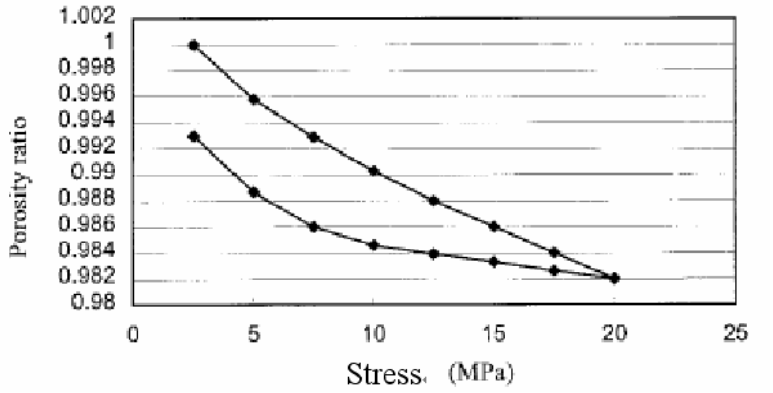

Figure 3-14: Relationship of Porosity Ratio and Effective Overburden Stress for Core 52

(After Chen *et al.* 2002)

Similarly, Figures 3-15 through 3-17 show the behavior of permeability k relative to initial permeability k_0 under varying effective overburden stress σ' for all three cores. Decrease of relative permeability with increasing effective overburden stress (corresponding to the decrease of formation pore pressure) and recovery of permeability with decreasing effective overburden stress (corresponding to the increase of formation pressure) are shown for all three cores. Hysteretic response to loading and unloading can also be observed for core 20 and core 39.

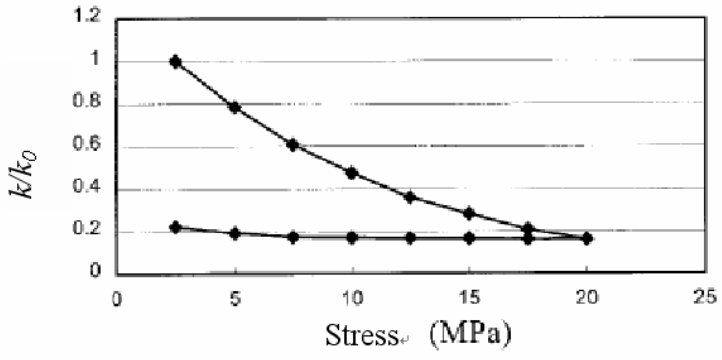

Figure 3-15: Permeability Ratio and Effective Overburden Stress for Core 20

(After Chen *et al.* 2002)

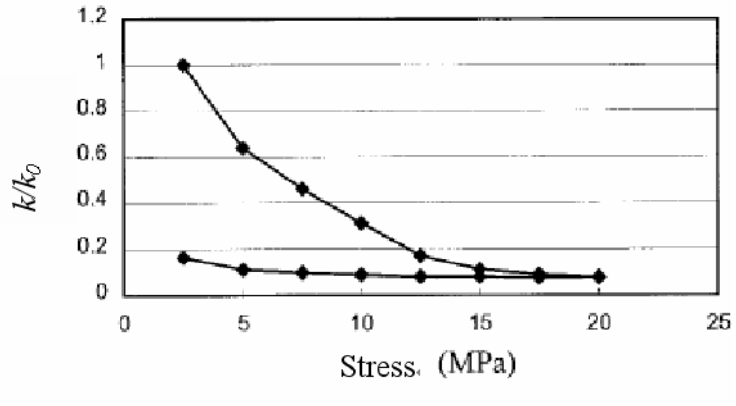

Figure 3-16: Permeability Ratio and Effective Overburden Stress for Core 39

(After Chen *et al.* 2002)

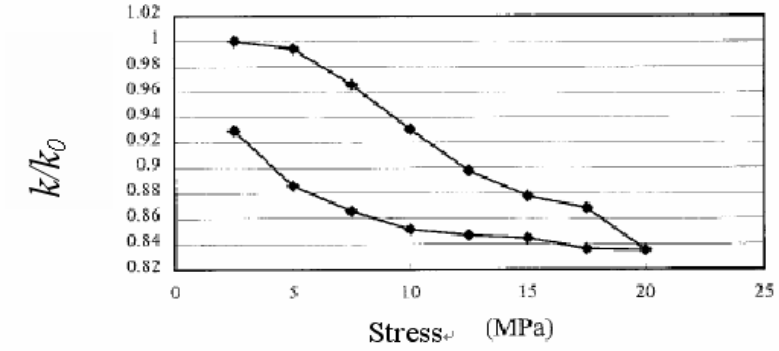

Figure 3-17: Permeability Ratio and Effective Overburden Stress for Core 52

(After Chen *et al.* 2002)

Pore size distribution under changed effective overburden stress is illustrated in Figure 3-18, Figure 3-19, and Figure 3-20. All the three samples evidence a shift of pore sizes toward smaller pore size direction (characterized by smaller T_2 value) when effective overburden stress increases. Pore sizes distribution cannot recover to its initial level when effective overburden stress decreases to initial state.

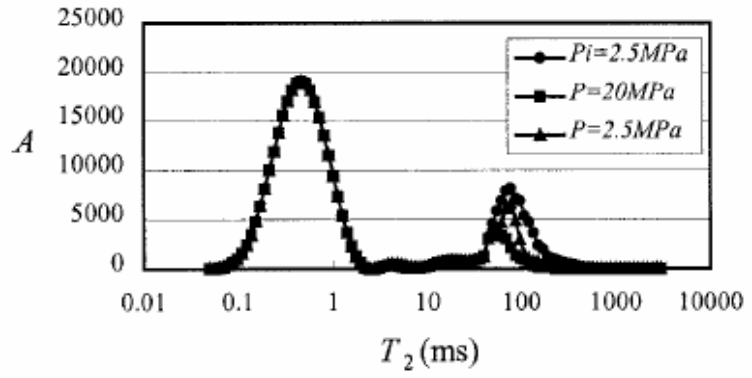

Figure 3-18: Changes in Relaxation Time with Effective Overburden Stress of Core 20

(After Chen *et al.* 2002)

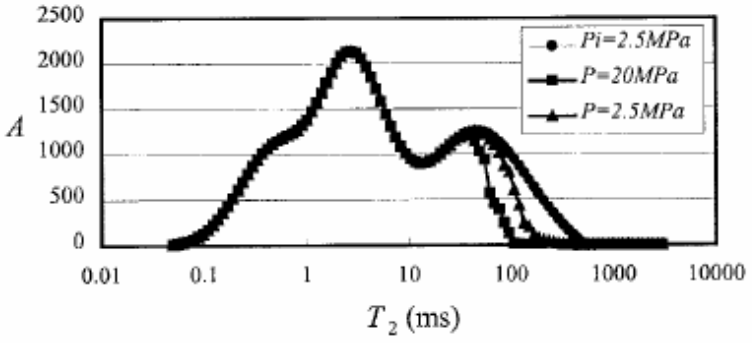

Figure 3-19: Changes in Relaxation Time with Effective Overburden Stress of Core 39

(After Chen et al. 2002)

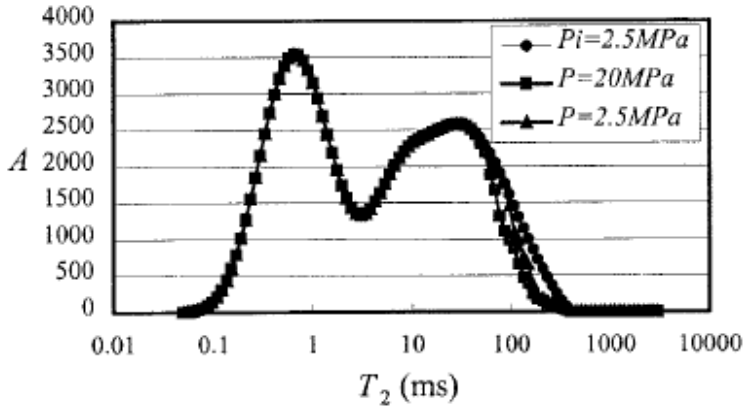

Figure 3-20: Changes in Relaxation Time with Effective Overburden Stress of Core 52

(After Chen *et al.* 2002)

From the observations of the pore size distribution, the mechanisms of pressure-dependent porosity and permeability change can be deduced. When formation pressure decreases, the distribution of pore sizes was shifted toward smaller radii. Then, with the increase of formation pressure, porosity, pore size distribution, and permeability recovered gradually, but did not return to the original values. The recovery of porosity and permeability was less in the fractured cores compared with the unfractured ones, as the contribution of fractures to permeability is larger than that of pores.

Mainly plastic deformation (irrecoverable) takes place in fracture deformation, while matrix pores mainly show elastic deformation (recoverable). The permeability of the formations with fractures can decrease substantially during formation pressure decrease associated with production, and may not recover during formation pressure increase. It is very important to keep an appropriate formation pressure during the exploitation of petroleum, not only as a driving force, but also to sustain good reservoir flow properties.

Chan (2004) carried out a similar research program on the influence of stress change on porosity and permeability for core samples from Gulf of Mexico Field X. Laboratory experiments on stress dependency of porosity and permeability for samples collected from Gulf of Mexico Field X are shown in Figure 3-21 and Figure 3-22. All samples demonstrate porosity and permeability diminution with effective confining stress increase. At the

beginning of effective stress increase, the decrease of porosity and permeability decrease as a result of closure of micro-fractures and small pores. After that, the decrease rate of porosity and permeability slowed down. When the effective confining stress increases to a certain extent, coalescing of small fractures and pores causes the collapse of matrix structure of samples, and a faster decrease of porosity and permeability can be observed.

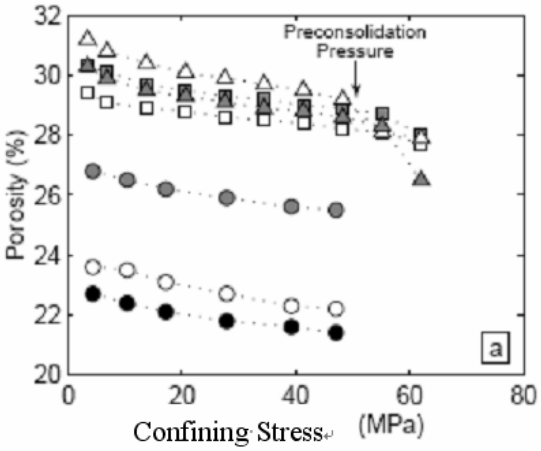

Figure 3-21: Laboratory Experiments on Porosity Variation with Confining Stress for Samples from Gulf of Mexico Field X

(After Chan *et al.* 2004)

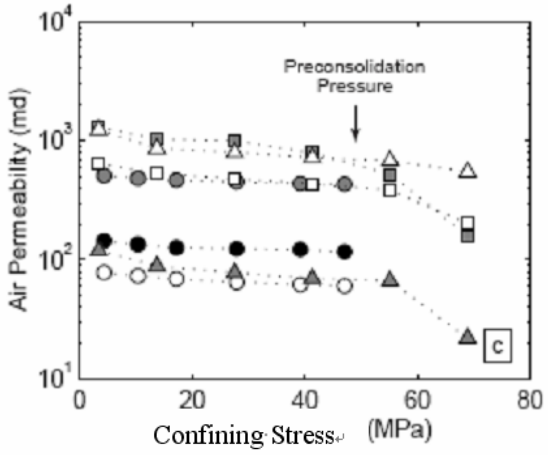

Figure 3-22: Laboratory Experiments on Permeability Variation with Confining Stress for Samples from Gulf of Mexico Field X

(After Chan *et al.* 2004)

3.6 Unstable Flow In Heterogeneous Porous Media

Heterogeneous porous media are characterized by micro-heterogeneity. That means significant natural variations in permeability in the flow field. Heterogeneity of porous media may cause unstable flow to develop (fingering), and the phenomenon of fingering can often be observed directly. Greenkorn *et al.* (1988) defined heterogeneity as a region of different permeability in the flow field. He used the ratio of size, length, and permeability to describe heterogeneity. Heterogeneity will affect capillary forces, flow state, sweeping efficiency, as well as recovery rate.

Tanzil *et al.* (2002) introduced an experiment to observe foam mobility in homogeneous and heterogeneous sand-packed columns. The differences (induced heterogeneity) arise because of the generation of foam lamellae by snap-off for flow across an abrupt increase in permeability. This mechanism is shown to be dependent on the degree of permeability contrast and the gas fractional flow. It has important implications for the degree of gravity segregation of gas and liquid in field-scale recovery processes.

Most recent analysis works use modeling and numerical simulation methods to study unstable flow in heterogeneous porous media (Paterson *et al.* 1998, Jenny *et al.* 2002, Zhang *et al.* 2000). Jenny *et al.* (2002) introduced a modeling method for flow analysis in complex porous media. The method used a hexahedral multi-block grid formulation for the modeling of two-phase reservoir flow. The method was applied to a realistic example involving flow through a heterogeneous system. More variation in well inflow with position than in the homogeneous case was observed because of the variation in permeability along the well trajectory. Paterson (1998) used network models to investigate the effect of correlated heterogeneity on capillary-dominated displacements in porous media. The network was composed of pores and throats. Reservoir heterogeneity was described by using the Fractional Brownian Motion method. The network models reproduce the experimental observation that relative permeability is greater in the direction parallel to the bedding compared with perpendicular to the bedding.

Zhang *et al.* (2000) used a stochastic approach to quantitatively study the uncertainty in flow performance predictions due to uncertainty in the reservoir description. They treated permeability as a random space function and flow velocity as random fields. They used a Lagrangian framework to deal with the transport problem. Their results suggested that the statistics of the flow-related quantities display smaller variability compared to those of the input statistics of static properties such as permeability. Modeling and numerical simulation method offer convenient and easily applicable means of studying unstable flow in heterogeneous porous media, but some issues still remain. Network and multi-block grid methods are difficult to represent situations when wells are oriented in a direction skewed to the grid (neither parallel nor perpendicular). A lot of further research is needed for easy application of the stochastic approach.

To cope with heterogeneity, or to decrease heterogeneity influences, several means can be used. One is to adopt separated layer injection and production such as in Daqing Oilfield. Sometimes selective perforation and fracturing will help. The most commonly used method is “Conformance Control” either using cross-linked gel or uncross-linked gel. Thompson *et*

al. (1999) introduced a conformance control technique in which gel is placed into a heterogeneous porous medium by first injecting a high-viscosity non-cross-linked polymer solutions and second, a low-viscosity cross-linked polymer. The fluid diversion was achieved in a dual-zone medium with a 4:1 permeability ratio. Less distinct fingers and a nearly plug-flow displacement were observed.

The above modeling and numerical simulation methods are mainly linear elastic flow models that can be described by Darcy's law, whereas actual fluid flow in porous reservoir under development is coupled with mechanical response of the reservoirs. Nonlinear mass balance equations for fluid are subjected to Darcy's law and nonlinear equilibrium equation for matrix and fluid compressibility must be taken into consideration.

3.7 Summary

Reservoir heterogeneity can be broadly classified as mega-heterogeneity, macro-heterogeneity and micro-heterogeneity. Macro-heterogeneity can be further divided into horizontal heterogeneity and vertical heterogeneity. Reservoir mega-heterogeneity can be described by reservoir geometry, reservoir faults distribution, and fracture and folding development. Reservoir macro-heterogeneity is not too difficult to understand, to characterize, and to take measures to handle it. Micro-level heterogeneities are not so easy to identify.

Reservoir mega-heterogeneity in Daqing Oilfield is not severe: the overall geometry is simple and the structure is flat with no more than 6° limb dip angle and low curvature (folding). Faults are numerous and appear to be evenly distributed, and no large-scale fractures and folds were found. Large area casing shear has no apparent relationship with mega-heterogeneity factors.

Macro-heterogeneity is, however, severe in Daqing Oilfield. Horizontal heterogeneity is characterized by various different depositional facies which can then be subdivided into micro-facies such as channel facies, delta inner front facies, and delta outer front facies. Sand body geometries, distribution dimension and physical properties among the facies vary

greatly. Vertical heterogeneity of Daqing Oilfield is characterized by up to 100 individual sand layers with thickness ranging from 0.2 meters to 20 meters and a permeability range from 20 to 1600 mD (average 230 mD). Furthermore, there are a number of stacked sand-silt-shale sequences.

Combining mercury porosimetry and photo-micro-graphic analysis can lead to a better understanding of pore accessibility and pore structure characterization. By using the method, a complete pore size distribution of a range of several nanometers to several thousands of micro-meters can be obtained. Also, cumulative pore volume distribution and pore-throat aspect ratio can be deduced.

Fractal dimension can be used to describe the heterogeneity of pore structure. The larger the fractal dimensions of the pore structure, the more heterogeneous the pore structure for sandstones.

Effective overburden stress changes as a result of formation pore pressure change. Effective overburden stress change can cause variation of pore porosity, permeability, and pore-size distribution. Hysteretic behavior can be observed. When increases in effective overburden stress take place, porosity and permeability will decrease. Porosity and permeability will not recover to their initial value even when effective stress was lowed to initial level. Pore size distribution under changed effective overburden stress behaves a shift of pore sizes toward smaller pore size direction when effective overburden stress increases. Pore sizes distribution cannot recover to its initial level when effective overburden stress decreases to initial state.

Reservoir sandstones of Daqing Oilfield have similar porosity and mineralogy. Their micro-heterogeneity lies in considerably varied micro-structure. The difference in micro-structure affected permeability, which varied considerably and affects micro-scale anisotropy, which showed a strong directional dependence. Heterogeneous porous media will cause unstable flow and unevenly distributed pressure systems.

Chapter 4
Coupled Geomechanics and Reservoir Flow Modeling

4.1 Introduction

Reservoir geomechanics is about simultaneous study of fluid flow and mechanical response of the reservoirs, and this is important, as demonstrated in the previous chapter. It combines aspects of rock mechanics, *in situ* stress determination, fluid flow, and fault and fracture analysis. Reservoir geomechanical models are used to quantitatively analyze problems such as fluid flow through fractured reservoirs, compaction drive, water flooding, surface subsidence, hydrofracturing, sand production, fault seal, wellbore and casing stability, and prediction of reservoir responses to production.

Fluid production or injection in a hydrocarbon reservoir results in decreasing or increasing of fluid pressure as well as increasing or decreasing of effective overburden stress on reservoir rock. The increase (or decrease) in effective overburden stress will in turn compact (or dilate) the reservoir rock and change the stress state in the reservoir. As the fluid flows through the porous media, its mechanical effect is witnessed by effective stress change.

The first attempt to describe fluid-solid coupling in a deformable porous medium was done by Terzaghi before 1943 (Terzaghi 1943). He initially had developed the concept of effective stress and consolidation for incompressible solid grains. Later on, M.A. Biot established the general theory of three-dimensional consolidation with the basic principles of continuum mechanics and extended poroelastic theory to anisotropic and nonlinear materials (Biot 1955, 1956, 1957, 1962, 1973). Ghaboussi and Wilson (1973) introduced fluid compressibility to the consolidation theory. Several authors have presented the mathematical formulation for modeling poroelastic multiphase flow (Tortike and Farouq 1987, Ghaboussi and Wilson 1973, Settari and Mourits 1998, Wang and Lu 2001, Thomas *et al.* 2002, Gai *et*

al. 2003). Mourtis (1994 and 1998), Thomas (2002) and Gai *et al.* (2003) describe an iteratively coupled model that employs parallel computing.

In this chapter, I will discuss the basic theories of fluid flow in deformable porous media, and compare different coupling techniques. I will also discuss the finite element method for solving complex partial differential equations.

4.2 Fluid-Flow Theory in Deformable Porous Media

Fluid flow around a structure gives rise to forces and associated motion of the structure, which again influences the fluid flow. The governing equations for the interaction of a fluid phase with a deforming porous medium are formulated on the basis of generalized Biot's theory and include both fluid flow and solid deformation. Macroscopic mass balance law suitable for describing the physics of the porous medium mixture can be formulated by application of volume averaging techniques.

4.2.1 Fluid Flow

Most commonly formulated equations are based on the basic principle of fluid mass conservation and Darcy's relationship. A nonlinear mass balance equation for fluid flow is subjected to Darcy's law and nonlinear equilibrium equations that take into account the effects of matrix and fluid compressibility. Taking single-phase fluid flow as an example, the mass conservation equation is as follows:

$$\nabla\left(\rho_f v\right)+\frac{dm}{dt}=w \qquad (4.1)$$

where m is the variation in fluid mass content; dm/dt is rate of change with time; v is fluid macroscopic; ρ_f is fluid density; ∇ stands for divergence; and, w is a source term corresponding to wells in the field, positive for injectors and negative for producers.

Change in rate of fluid mass can be calculated through the following equation including both matrix and fluid compression:

$$\frac{dm}{dt}=\rho_f(c_m+\phi c_f)\frac{dp_f}{dt} \qquad (4.2)$$

where ρ_f is fluid density; c_m is the compression coefficient of the rock matrix; c_f is fluid compression coefficient; ϕ is rock porosity; and p_f is fluid pressure.

Darcy's law can be written as follows:

$$\nabla(\rho_f v) = -\nabla \cdot \left[\frac{k\rho}{\mu} (\nabla p_f - \rho_f g \nabla H) \right] \qquad (4.3)$$

where k is rock permeability; ρ_f is fluid density; μ is fluid viscosity; p_f is fluid pressure; g is acceleration of gravity; and H is depth calculated from a certain datum plane, downwards positive.

4.2.2 Solid Deformation

Three forces act on the solid matrix when there is fluid flow through a porous medium. They are: the solid weight, the buoyancy, and the drag force (Terzaghi 1943). Taking these forces into account, an overall momentum balance equation governing mechanical response of the coupled system can be given as below:

$$\Delta\sigma + \rho g + p_f = 0 \qquad (4.4)$$

where σ is total stress; ρ is the total density; p_f is fluid pressure.

Total density of the system is computed using following relation:

$$\rho = \rho_f + (1 - \phi)\rho_m \qquad (4.5)$$

where ρ_f is fluid density; ρ_m is solid density; ϕ is porosity.

4.2.3 Constitutive Equations

Determining the displacement of the block (i.e. relative inter-block deformations) is the most important component of casing deformation mechanism studies. If the rock is affected by the long-term high-pressure injection, its mechanical characteristic changes. Constitutive equations provide essential relationships between various macroscopic and microscopic properties of a continuum. They also determine the degree of nonlinearity, which has a direct bearing on subsequent phases of mathematical analysis development.

Constitutive relations for flowing fluids in porous media are usually given by density relations and are termed as equations of state (Jha 2005).

$$c_f = \frac{1}{\rho_f}\frac{d\rho_f}{dp} \qquad (4.6)$$

where c_f is conventionally taken to be constant with respect to pressure.

Deformation of the solid phase depends on the effective stress, and deformability is linked to skeleton nature and fabric, strain, and material specific properties. Formations will creep and slide when affected by long-term high-pressure injection, and this is a nonlinear process. Rock deformation in the sliding zone is not elastic deformation. Constitutive equations can be written as a scaled-up stress-rheological model (Ortoleva 1994), which can more correctly characterize the deformation behavior.

$$\varepsilon = \frac{\sigma}{E} + \frac{\sigma^N t}{\eta} \qquad (4.7)$$

where ε is the amount of rock deformation; N is a lithologic constant; E is Young's Modulus; η is the coefficient of rock viscosity; and t is time.

4.2.4 Initial Condition and Boundary Condition

In most cases the initial conditions are:

$$\rho_f = \rho_{f0} \qquad (4.8)$$

$$p_f = p_{f0} \qquad (4.9)$$

$$\sigma = \sigma_0 \qquad (4.10)$$

where ρ_f is fluid density; ρ_{f0} is initial fluid density; p_f is fluid pressure; p_{f0} is initial fluid pressure; σ is stress; and σ_0 is initial stress.

If we use $\mathbf{\Omega}$ to denote the domain of interest, **n** to denote the unit outward normal vector on $d\,\mathbf{\Omega}$, and **v** to denote Darcy's velocity vector, the boundary condition will be:

$$\mathbf{v}\,\mathbf{n} = 0, \text{ on } d\,\mathbf{\Omega}. \qquad (4.11)$$

4.3 Finite Element Formulation

The development of finite-element formulation methods can be traced back to the early 1940's when Hrennikoff and Courant initiated their work for solving complex elastic structural analysis problems in civil engineering and aeronautical engineering. Although approaches used by earlier engineers are dramatically different, they share one essential characteristic: mesh discretization of a continuous domain into a set of discrete sub-domains. Courant divided the domain into finite triangular subregions for solution of second-order elliptic partial differential equations (PDEs). The full development of the finite element method began as early as late 1950's for airframe and structural analysis. In the 1960's the method began to be used in civil engineering. Since the 1970's, the method has been applied for modeling of physical systems in a wide variety of engineering disciplines such as fluid dynamics in petroleum industries, especially in the modeling of reservoir geomechanics (Ghaboussi and Wilson 1973, Tortike and Ali 1987, Settari and Mourits 1998, Settari and Walters 1999, Wang and Lu 2001, Thomas *et al.* 2002, Gai *et al.* 2003, Liu 2003, and Jha 2005).

The development of the finite element method in structural mechanics is often based on an energy principle, which provides a general, intuitive and physical basis. Mathematically, the finite element method (FEM) is used for finding approximate solution of partial differential equations (PDE). The solution approach is based either on eliminating the differential equation completely (steady-state problems), or rendering the PDE into an equivalent ordinary differential equation, which is then solved using standard techniques such as finite differences, etc. In solving partial differential equations, the primary challenge is to create an equation which approximates the equation to be studied, but which is numerically stable, meaning that errors in the input data and intermediate calculations do not accumulate and cause the resulting output to be meaningless. There are many ways of doing this, all with some advantages and some disadvantages. The Finite Element Method is a good choice for solving partial differential equations over complex domains or when the desired precision varies over the entire domain.

Generally, for the convenience of simplified settings in geomechanics, fluid-structure problems may end up with a partial differential equation (PDE) for the fluid flow and an ordinary differential equation (ODE) for the motion of the structure. After discretization in space and time, the linear system for coupled flow and geomechanics can be written as a compact 2 × 2 block system (Jha 2005). In order to facilitate the discussion of different degrees of coupling, considering first the general formulation of the coupled problem in a finite element setting, the following matrix system used by Settari and Walter (1999) were introduced:

$$[(K, L), (L^T, E)]\ [\Delta_t \delta, \Delta_t P]=[F, R] \qquad (4.12)$$

where K is the stiffness matrix, δ is the vector of displacements, L is the coupling matrix to flow unknowns, E is the flow matrix and P is the vector of reservoir unknowns (i.e., pressures, saturations and temperatures). On the right-hand side F is the vector of force boundary conditions and R is the right-hand side of the flow equations. The symbol Δ_t is the change over time step, i.e.

$$\Delta_t \delta=\delta^{n+1}-\delta^n,\ \Delta_t P= P^{n+1}-P^n \qquad (4.13)$$

Note that in the conventional reservoir simulation notation, $E = T - D$ where T is the symmetric transmissibility matrix, D is the accumulation (block diagonal) matrix, and $R = Q - TP^n$ where Q is the vector of boundary conditions (well terms).

4.4 Different Coupling Techniques

Coupling methods have been extensively used in the petroleum industry, and Phillips and Wheeler (2003) have analyzed theoretically the single-phase flow model, although iterative techniques can be generalized to multiphase flows.

For solving large systems of coupled equations, operators or time splitting has proved to be a useful approach and used extensively in the past decades. In Biot's poroelastic modeling, the operator splitting technique is used to design a loosely coupled scheme by separating the elasticity operator from the diffusion operator. Then, each field problem can be solved independently and efficiently by available iterative methods. The degree of coupling is

generally based on the time scale and how often the two distinct models exchange information. More specifically, time evolution is controlled by the flow model, and the degree of coupling depends on how often the displacement calculations are updated. Clearly, the choice of coupling scheme affects the stability and accuracy of the solutions as well as the computational efficiency. Sometimes trade-offs must be made to optimize the computer running time. Settari and Walter (1999) discussed the different coupling methods and categorized them as decoupled, explicitly coupled, iteratively coupled and fully coupled.

4.4.1 Fully Coupled Techniques

A fully coupled approach solves two field equations simultaneously using the same discretization. The method is unconditionally stable in time and optimally accurate in the energy norm for displacements and second-order accurate for pressure and velocities. However, its practical usefulness is limited by the fact that special linear solvers are required to handle the fully coupled system. This makes the coupling of two existing complex individual models even more complicated, especially if one adds in thermal effects and phase changes such as steam condensation on a sharp temperature front.

4.4.2 Decoupled Techniques

In classical decoupled techniques, the fluid flow equations are completely decoupled from the poroelastic model by assuming $d\sigma = 0$. Porosity changes are approximately caused only by pore pressure changes via rock compressibility. Hence, these methods do not account for the global effective stress and total stress response to changes in pore pressures.

If we combine equation 4.12 and equation 4.13 and suppose there is no stresses change, i.e. $d\sigma = 0$, fluid flow equations are completely decoupled from the poroelastic model and the following matrix equation can be used.

$$[T\text{-}D]\,\Delta_t P = Q - TP^n \qquad (4.14)$$

Once the pressure has been solved, displacement may be obtained whenever necessary.

$$K\Delta_t \delta = F - L\,\Delta_t P \qquad (4.15)$$

4.4.3 Explicit Coupling

Explicit coupling is essentially a staggered partitioning method. It is achieved by lagging coupling terms in one or more time steps. Generally, quasi-static behavior is assumed for geomechanics models. Different time steps may be used for displacement and flow calculations respectively.

If the same time scale is used for flow and displacement, the explicit coupling technique involves the solution of the following decoupled system:

$$[T\text{-}D]\,\Delta_t P^{n+1} = Q - TP^{n} - L^{T}\Delta_t \delta \qquad (4.16)$$

$$K\Delta_t \delta^{n+1} = F - L\Delta_t P^{n+1} \qquad (4.17)$$

The explicit coupling is a special case of the iteratively coupled system in which only one iteration per time step is performed.

4.4.4 Iterative Coupling

Iterative coupling method is a tightly coupled scheme designed primarily for nonlinear problems. In an iteratively coupled scheme, repeated solutions for multiphase flow and poroelasticity equations are coupled through nonlinear iterations in each time step. If n denotes time step and k denotes nonlinear iteration, an iterative method involves the repeated solution of the following system in each time step $n + 1$, the matrix equations are as follows:

$$[T\text{-}D]\,\Delta_t P^{k+1} = Q - TP^{n} - L^{T}\Delta_t \delta^{k} \qquad (4.18)$$

$$K\Delta_t \delta^{v+1} = F - L\Delta_t P^{v+1}, \quad (v=1, \ldots n \text{ steps}) \qquad (4.19)$$

$$\Delta_t \delta^{v} = \delta^{v} - \delta^{n}, \; \Delta_t P^{v} = P^{v} - P^{n} \qquad (4.20)$$

Advantages of this method include:

1. Stability and accuracy. It can produce the same results as a fully coupled technique if a sufficiently tight, nonlinear convergence criterion is enforced.
2. Modularity feature. It allows coupled equations to be processed by separate program modules, taking advantage of specialized features and disciplinary expertise built into independently developed single-field models, combining the vast simulation experience in

the diffusion domain with the vast experience in the stress-strain domain without a direct coupling of all the equations.

4.5 Summary

The multi-component nature of reservoir rock requires descriptions of both pore fluid and solid components. Fluid flow in deformable porous media can be described by governing equations for fluid flow and governing equations for solid deformation. Governing equations for fluid flow include mass conservation equation (Equation 4.1) and Darcy's law (Equation 4.2). Solid deformation can be governed by overall momentum balance equation (Equation 4.4). Constitutive relations for flowing fluids in porous media are given by density relations, whereas constitutive equations for deformation of the solid phase are given as scaled-up stress rheological models.

On discussing mathematical models for coupled geomechanical simulation, the summarized equations are subjected to discretization techniques. Governing equations, constitutive equations, initial conditions, and appropriate boundary conditions in the discretized system provide an equation set. Primary unknowns of the system are determined by the numerical finite element process.

Among many different coupling techniques, iterative coupling method is used most frequently because of its stability, accuracy, and modularity features.

Chapter 5
Simulation of Large Area Casing Shear

5.1 Introduction

As discussed in the previous chapter, fluid flow in deformable porous media influences local stress fields. In other words, production and injection activities will induce changes in the natural stress fields during the period of oilfield development. Much research has been carried out on production-induced stress and the influence on reservoir compaction (Li 1995, Fredrich 1998 and 2000, Ibekwe 2003, Chan 2004). There are few reports on injection-induced stress fields and the consequences on oilfield development. In the development of Daqing Oilfield, the period of compaction production was very short because of the early injection policy to maintain reservoir pressure. As a result, casing loss issues were not serious at that time. It is only after relatively longer periods of full oilfield-wide water injection that casing shear became a serious problem and remains serious till today. Therefore, studying and modelling injection-induced stress and its consequence on casing stability is of special importance.

In this chapter, a case study is introduced, and an *in situ* experiment of an injection-induced stress field is presented. Simulation results based on the *in situ* experiment are also presented, and thereafter the casing shear mechanism with respect to injection-induced stress fields is revisited.

5.2 Far-Field Stress Field

Daqing Oilfield is in the centre of Songliao Basin, as stated in Chapter 1. During the geological history of the basin's evolution, it has once undergone nearly East–West extensional stresses, so that the maximum horizontal stress σ_H (or σ_1) was nearly in the North-South direction at that time. That is why faults in Daqing Oilfield are all normal faults

and most major faults are NW-SE azimuth (refer to Figure 5-1). Then in Cenozoic time, the whole China Continental Plate was subject to compression between the Pacific Plate and the Indian Plate, confined by the Philippines and Siberia Plates. The basin is compressed in nearly an E-W direction stress. Figure 5-2 sketches the deformation of the plates. The Pacific and Indian Plate advance at a speed of several millimetres per year. The tangent of particular points along the dashed line in the figure indicates the direction of maximum horizontal stress of that point (Li *et al.* 1997).

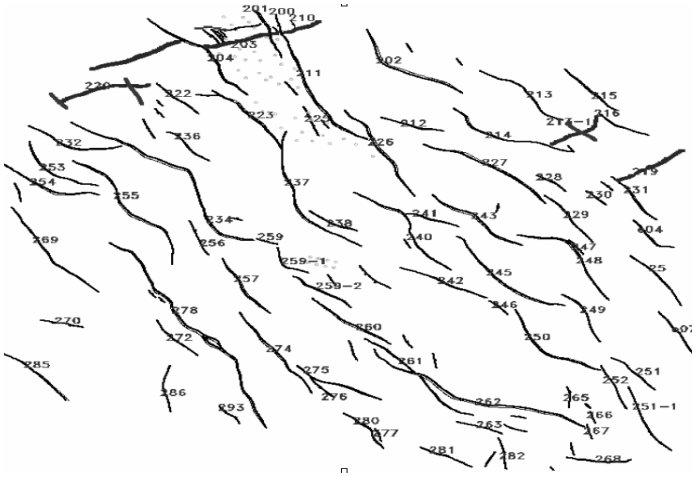

Figure 5-1: Distribution of Faults in Northern Xingshugang Area of Daqing Oilfield

Figure 5-2: Sketch Map Showing the Deformation around China Continental Plate

(After Li *et al.* 1997)

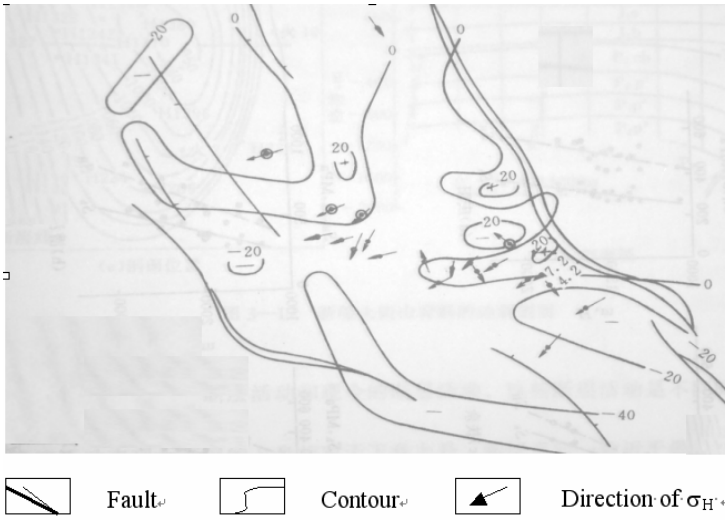

Figure 5-3: Direction of σ_H Indicated by Down-Hole Lead Moulds

(After Li *et al.* 1997)

From Figure 5-2, we can get an approximate maximum horizontal stress direction that is around N80°E. Casing deformation data also indicate a similar direction of maximum horizontal stress (as shown in Figure 5-3). Figure 5-3 is the map showing the casing deformation direction as an indication of *in situ* maximum horizontal stress direction. The map was drawn based on down-hole lead moulds taken in casing deformed wells in 1986. The direction of the shorter diameter of lead moulds was thought to be the maximum horizontal stress direction of the *in situ* stress field. The dominant casing deformation direction gives approximately a N80°E direction.

Because of the changing of stress field in geological time ("pull" followed by "push"), most faults in the oilfield establish a "chair" shape (Figure 5.4). No thrust faults are found, but formations shapes near faults are changed due to the "Pull-Push" event. Local increase in thickness of formations near faults can be observed.

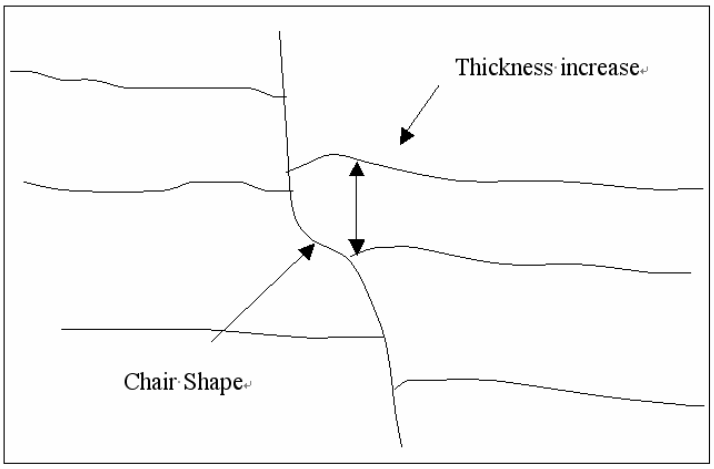

Figure 5-4: Sketch Map of Fault shape in Cross Section

Li *et al.* (1997) give a calculation equation of the magnitude of far-field stresses in Songliao Basin based on large amounts of hydraulic fracturing stress measurement data (Equation 1.1-1.3 in Chapter 1). According to the equations, the far field stresses of reservoirs between depths 700m to 1200m in the oilfield are as follows:

$$\sigma_H = 16.26 \sim 29.55 \text{ MPa} \quad (5.1)$$

$$\sigma_h = 11.99 \sim 21.12 \text{ MPa} \quad (5.2)$$

$$\sigma_v = 14.70 \sim 25.20 \text{ MPa} \quad (5.3)$$

Therefore, in Daqing Oilfield, the stress regime is a type of strike-slip fault regime, i.e. $\sigma_H > \sigma_v > \sigma_h$. The tectonic movements formed many faults in the oilfield (refer to Figure 5-1) and these faults divided the reservoir into many fault blocks. The fault blocks, together with the heterogeneous reservoir properties, can lead to different formation pressures in water injection and production activities. Block pressure difference is one of the key factors causing large area casing shear.

5.3 *In situ* Experiment for Induced Stresses

In order to understand the disturbance effect of the injection pressures on the original stress field, an experiment was carried out to probe the influence of injection pressure changes on a local stress field. The procedure is described as this: injection wells in W1-3 injection wells

row and two stress monitoring wells (P1-1-7, P2-2-5) in the experimental area were chosen as the experimental group (as shown in Fig 5-5). First, the injection pressure of injectors in W1-3 row was lowered from 10.27 to 8.00 MPa and maintained for nine days. After 42 hours, measurements in well P1-1-7 indicated 0.02 mm displacement in the N15°W direction. In P2-2-3, the displacement was 0.01 mm 70 hours after the pressure drop. The maximum principal stress (σ_{HMAX}) direction is N83°E, very close to the regional σ_{HMAX} direction (N80°E).

The next step was to raise the injection pressure in well row W1-3 for nine days. The average injection pressure increased from 8.00 MPa to 12.00 MPa. The observed maximum displacement of P1-1-7 was 0.06 ~ 0.08 mm after 10 days and the σ_{HMAX} direction changed to N79°W. As for well P2-2-3, 16 days after this pressure increase, the borehole diameter at the measuring point was compressed by 0.05 ~ 0.06 mm, and the σ_{HMAX} direction was N80°E (Fig 5-5, where $\sigma_{HMAX} = \sigma_1$).

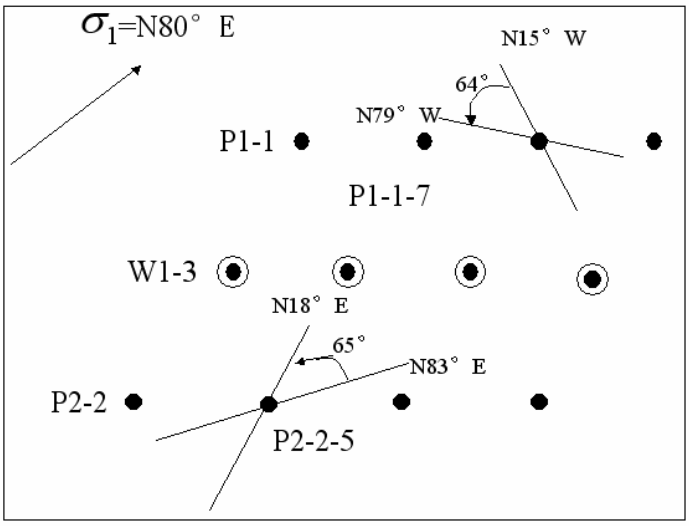

Figure 5-5: Sketch Map of Well Positions

● : Production well; ◉: Injection well. P1-1 and P2-2 are production wells rows. W1-3 is an injection well row. (Not drawn to scale).

The above experiments indicated that the variation of injection pressure has some obvious effects on the regional deformation and therefore stress field. Furthermore, the more injection pressure changed, the bigger the strain magnitude. The result also showed that the impact of injection well row orientations with respect to the regional stress field could not be neglected. The regularly spaced injection and production well rows induce enough pressure difference to drive strata creep and shear. The induced creep in the weak shale and the induced shear displacement field are the fundamental reasons for the serious casing deformation observed in this area of Daqing Oilfield.

5.4 Mathematical Equations Used for the Model

According to the above conceptual model, a mathematical model of large-area casing deformation was developed in order to simulate the stress field, the strain field, and the displacement field in areas of casing deformation occurrence. A stability coefficient range for the block was also developed.

From a micro-structure point of view, injection activity impacts the matrix through pore pressure, and causes expansion and shrinkage of the matrix. This, in turn, causes perturbation to the stress field in and around the block (variation of size and direction). In fact, stress and pressure changes are interactively coupled. At the same time, stress will directly impact fluid pressures in the pores of rock. In strata developed by high-pressure injection, there is always this coupling between the stresses and pressures. The mathematical model of large-area casing deformation must take into consideration of coupling effects in stresses and pressures (Tan 2001).

5.4.1 Nonlinear Mathematical Equation

Fluid flow in porous media underground follows Darcy's law (Whiteker 1966). However, fluid flow in porous media under coupling effects of tectonic stress and fluid follows a nonlinear equation. According to the analysis in the previous chapters, the following equation can be developed from equations (4.1-4.3):

$$\rho_f(c_m+\phi c_f)\frac{dp_f}{dt}-\nabla\cdot\left[\frac{k\rho}{\mu}(\nabla p_f-\rho_f g\nabla H)\right]=w \qquad (5.4)$$

where k is rock permeability; ρ_f is fluid density; μ is fluid viscosity; p_f is fluid pressure; g is acceleration of gravity; H is depth calculated from a certain datum plane, downwards is positive; c_m is the rock matrix compression coefficient; ϕ is rock porosity; c_f is fluid compression coefficient; and, w is a source term corresponding to wells in the field, positive for injectors and negative for producers. The above hydrological geology parameters' values can be obtained from either laboratory experiments or field *in situ* experimental data (i.e. calibration). Viscosity in the above equation can be calculated from the following formula (Yukler *et al.* 1978; Ungerer *et al.* 1990):

$$\mu=(5.3+3.8(AT)-0.26(AT)^3)^{-1} \qquad (5.5)$$

$$AT=(T-150)/100$$

where T is strata temperature. The formula to calculate the density is:

$$\rho_f=\rho_{f_0}[1-c_f(p_f-p_{f0})] \qquad (5.6)$$

where ρ_f is the reference value and ρ_{f0} is fluid density under condition of $p_f = p_{f0}$.

The formula for calculating the rock matrix compression coefficient c_m is:

$$c_m=-\left(\frac{\frac{d(\Delta h)}{\Delta h}}{d\sigma_h}\right) \qquad (5.7)$$

where h is rock thickness, Δh and $d(\Delta h)$ can be calculated according to the 3-D geodetic leveling, and σ_h is effective minor horizontal stress.

5.4.2 Stress Equilibrium Equation

In three dimensions, stresses at any point in the fluid-containing porous medium must satisfy the following equation：

$$\sum_{j=1}^{3}\frac{d\sigma_{ij}}{dx_j}+g\rho\,\delta_{i3}+p_f=0 \qquad (5.8)$$

where ρ is rock mass density and the number 3 represents the vertical direction.

The rock mass density ρ can be calculated through:

$$\rho = \phi\rho_f + (1-\phi)\rho_m \tag{5.9}$$

where ρ_m is rock matrix density.

5.4.3 Rheological Equation for Scaling-up of Stress

In an oilfield subjected to high-pressure water injection, there is intimate coupling among the tectonic deformation, rock, fluid, and terrestrial heat. Considering strain mechanics, a scaling-up rheological stress model (Ortoleva 1994) was used to characterize the deformation of rock. The overall strain velocity can be expressed as follows：

$$\varepsilon = \sum_i \varepsilon^{(i)}(\sigma, p_f, \theta, T) \tag{5.10}$$

where ε is the overall strain velocity, σ is stress, p_f is fluid pressure, θ represents rock structure variables, and T is temperature. This formula merely stipulates that rock strain processes are a coupled function of stress, fluid pressure, rock structure, and temperature.

5.4.4 Rock Mass Conservation Equation

A rock mass conservation equation can be written as

$$\frac{d\phi}{dt} = (1-\phi)\varepsilon \tag{5.11}$$

In this equation, suppose the solid grains are incompressible; then tectonic deformation and rock porosity are approximately related by the empirical equations.

$$k = 0.2\phi^3 / \left[S_a^2(1-\phi)^2\right] \quad \text{when } \phi \geq 0.1 \tag{5.12}$$

$$k = 20\phi^5 / \left[S_a^2(1-\phi)^2\right] \quad \text{when } \phi < 0.1 \tag{5.13}$$

In the above equation S_a is the specific area of rock grain in m^2/m^3. Because permeability affects the fluid flow, formula (5.11) expresses the coupling of tectonic deformation and fluid flux, through the change in porosity and the change of permeability.

The above relations (5.4), (5.8), (5.10), and (5.11) indicated that during the high pressure water injection period there would be an unavoidably strong coupling effect between the stress field and the fluid pressure (and flow). It is necessary to use equations (5.12) and (5.13) and relavant variables and relations to solve formulae (5.4), (5.8), (5.10), and (5.11). The finite element method is adopted to solve the above equation group.

5.4.5 Initial and Boundary Conditions

X1-3B area is taken as the investigation region (5.7 km^2). The shearing interval which was caused by high pressure water injection is composed of sliding layers, faults, and injection well rows. The top boundary of the interval was layer 1 (shale), the bottom was layer 5 (shale), east and west boundaries were two faults on the sides; south and north boundaries were given by injection well rows. The top, bottom, east, and west boundaries were all impermeable boundaries. The south and the north boundaries are specified to have a fixed flux. As for the stress field, a normal direction restriction was adopted for all directions. The earth's surface was left free, while the bottom was fully restricted.

According to the lithology of the area, the strata were divided into five lithologic zones. Hexahedron unit division was adopted, and each haploid has consistent lithologic parameters.

Rock mechanics parameters of the selected lithologies in the numerical model are listed in Table 5-1, quoted from the rock mechanic parameters measured by Petroleum University on 35 cores of 5 wells in the north area and middle area of Daqing Oilfield. The method of measurement was the triaxial test. There was no residual strength taken into consideration because the casing shear has mostly occurred at weak shale layers and no concentration of casing shear was observed along faults or along bedding planes (faults in the model are used only as boundaries). The main purpose of the simulation is to simulate casing displacement in the intact but weak shale layer, therefore triaxial measurement results of the rock mechanics parameters were used instead of residual strength test results from shearbox tests.

Table 5-1: Model Structure and Rock Mechanics Parameters of Various Lithologies

Layers and faults	Bottom depth (m)	E(GPa)		μ		c'(MPa)		ϕ(°)	
		Not water-affected	Water-affected	Not water-affected	Water-affected	Not water-affected	Water-affected	Not water-affected	Water-affected
Overburden	810~860	12~20	15~28	0.33	0.33			35~40	10~20
Layer 1	820~870	1.0	0.8	0.40	0.45	5.0	3.0		
Layer 2	880~930	20~22	12~16	0.25	0.30				
Layer 3	970~1020	12~14	8~10	0.21	0.36				
Layer 4	990~1040	30	22	0.25	0.30				
Layer 5	1300	1.2	1.0	0.4	0.42				
Fault 001		1.5		0.35		5.0		8~10	
Fault 002		1.5		0.35		5.0		8~10	

The original reservoir porosity and permeability parameters for the siltstone layers (layers 3-4) were calculated from geophysical log data from wells in basic well net (listed in Table 5-2). Parameters for each time step after initialization were calculated from the previous step.

Table 5-2: Porosity and Permeability Parameters Used for Siltstone Layers in the Modle

Well Id	Layer 1		Layer 2		Layer3	
	Porosity (%)	Permeability (mD)	Porosity (%)	Permeability (mD)	Porosity (%)	Permeability (mD)
X001	28.3	349	28.5	237	31.5	651
X002	24.9	164	25.9	47	28.3	258
X003	28.0	155	27.8	80	30.0	987
X004	27.3	119			28.3	396
X025			26.3	15	30.9	209
X125	24.3	53	20.8	22	25.3	50
X223	25.8	52			28.6	367
X225	28.9	315	26.9	176	27.2	180
X124	27.6	59			28.8	131
X127	24.7	20	27.5	97	28.2	316
X130			28.6	401	28.2	258
X228					28.0	493

Selected hydrological parameters are listed in Table 5-3. The parameters were obtained from laboratory experiments or from *in situ* experimental data. The original condition of the water-affected field in the studied area can be figured out according to the actually measured

water level data sometime before casing deformation through interpolation and fitting methods by making use of the fluid pressure of monitoring wells. As for the calculation time step thereafter, the calculated fluid pressure of the previous step was taken as its initial value.

Table 5-3: Hydrological Parameters for the Northern X1-3B Area

Parameters	Value
Rock mass density	2.7×10^{3} kg/m^{3}
Fluid density	1.05×10^{3} kg/m^{3}
Fluid compressibility coefficient	4.3×10^{-4} 1/MPa
Fluid viscosity	1.07 mPa·s
Acceleration of gravity	9.80 m/s^{2}

The reliability of the model was checked through the measured values from the observational network used in the field. The checking criterion is that the coincidence rate of the calculated casing deformation point and the measured point is more than 90%. The so-called coincidence refers to the condition that the error of calculated and measured casing deformation displacement is no more than one order of magnitude quantitatively and the displacement azimuth error is smaller than one quadrant. Although these seem to be lenient conditions, recall the great degree of heterogeneity in the reservoir. Also, only if the two conditions are fulfilled can the calculated and the measured value be considered coincident; otherwise not.

The original state of water invasion (extent, amount) in the study area can be deduced from actual measurements of water level data sometime before casing shear occurs, using interpolation and fitting techniques based on actual fluid pressure measurements in monitoring wells. For the iterative solution, this is the initial condition, and for solution steps, calculated fluid pressures are taken as subsequent initial values.

Validation of the model in practice was checked through measured values from the monitoring network. During the process of simulation, field experimental work was also carried out, and actual measured casing displacements and the azimuth of these displacements were compared with the simulation results, achieving a true field calibration.

5.5 Simulation Results

The numerical model of large-area casing deformation comprises formulae (5.4), (5.8), (5.10) and (5.11); it is subject to constitutive laws as well as defined initial and boundary conditions. In the extreme, these constitutive laws may include changes in parameters (strong non-linearity), varying boundary conditions with time, diffusion and stress-strain relationships (coupling), and will give an incrementally solved displacement field, which is the sum of strains. The problem solved and presented in this thesis is based on field and laboratory data, and addresses only mild non-linearity.

5.5.1 Simulation result analysis

Figure 5-6 illustrates the measured and simulated displacement values. When casing displacement is smaller than 80 mm, measured data and the simulation results are in reasonable agreement. When the actual casing displacement becomes larger than 80, the field data no longer tracked the simulation results: this represents a physical limitation on the measurement of the diameter of the casings (around 120 mm).

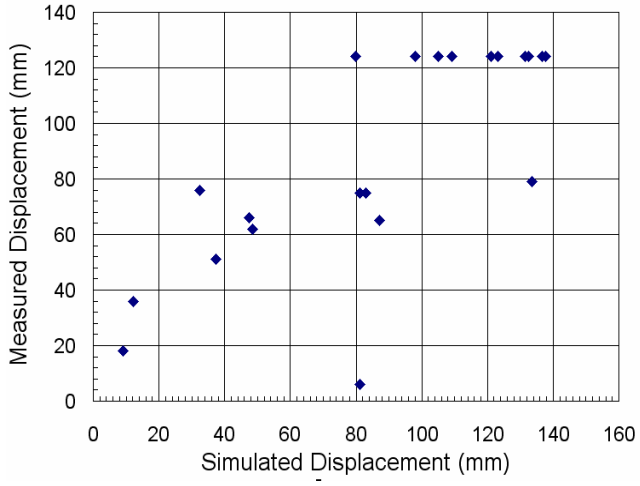

Figure 5-6: Measured Casing Displacement vs. Simulated Casing Displacement

Figure 5-7 gives the azimuth difference between measured and simulated displacements. Data points are plotted as measured azimuth minus simulated azimuth. Almost all the points (except 3 anomalous ones) fell in the range of no more than 90°, indicating that the

magnitude of the azimuth measurement error is smaller than one quadrant. Simulated results were coincident with the calculated results.

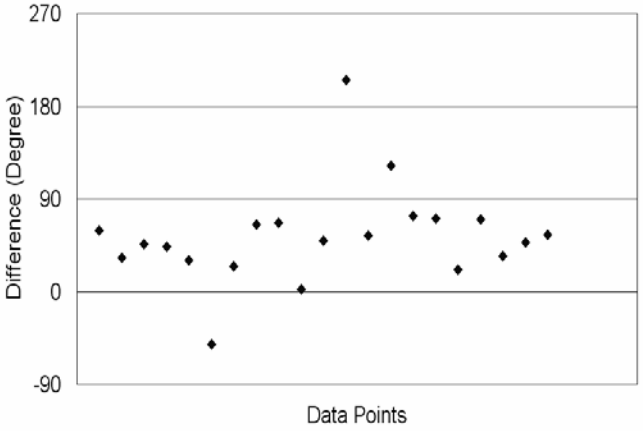

Figure 5-7: Azimuth Difference of Displacement between Measured Casing Displacement and Simulated Casing Displacement

Numerical simulation carried out in the study area indicated that variations in injection pressure induced a substantial perturbation on the local stress field. The induced stress fields associated with each injection well overlap with each other. Once the maximum compressive stress parallels or nearly parallels the differential pressure, the shear stability of the strata is severely compromised, and when the thrust stress imposed exceeds the shearing resistance, the strata will slip in a direction coaxial to the vector connecting high pressure to low-pressure areas. As a result, large areas of endemic casing shear will occur.

5.5.2 Determination of a Stability Coefficient

The stability coefficient (K) is defined as the ratio of average displacement (DIS) at a certain time to the displacement when large-area casing deformation takes place (DIS_e). That is,

$$K = \frac{DIS}{DIS_e} \tag{5.14}$$

where DIS_e represents the critical state when casing deformation will occur in a large area; it is calculated as the mean displacement of all nodes.

$$DIS_e = \frac{\sum_{i=1}^{n} DIS_i}{n} \tag{5.15}$$

where n is the number of nodes, and DIS_i is the simulated displacement of node i. When $K < 1$, the block is relatively stable, it is not likely that general casing shear will take place; when $K \geq 1$, the block is in an unstable state, and it is deemed that general detrimental casing deformation will likely occur.

The determination of DIS in the above formula is based on the numerical coupled simulation; as for DIS_e, it can be determined according to the critical state when shear deformation develops. The closer the monitoring data and performance data to the time of deformation occurrence, the better the data reflect the critical state of formation slippage.

By history matching, the simulated critical displacement was determined. The measured injection pressure and block pressure difference before deformation were 12.7 MPa and 0.86 MPa respectively.

5.5.3 **Scale Effects of Water-affected Shale Area**

Several scenarios were devised and simulated to calculate the stability coefficient of the formation under various injection pressures and block pressure differences. So long as the value was $K < 1$, large-area deformation of the block would not occur; therefore, according to the actual conditions of oilfield development, so long as the injection pressure is kept smaller than 12.7 MPa and the block pressure difference is controlled below 0.86 MPa, the probability of large-area casing deformation in this area is much less. This limit can be taken as a reference to other blocks having similar geological tectonic characteristics, although there may be differences arising because of parameters and geometry.

Under such injection pressure and pressure difference, how big would the water-affected region be to cause the areal casing deformation? Several scenarios were devised and simulated to calculate the stability coefficient of formation (Table 5.4). According to the simulation results, under certain injection pressure (12.7 MPa) and block pressure difference

(0.86 MPa), if the ratio of water-affected area to the total block area is smaller than 50%, the formation is in the elastic deformation stage with the value of $K < 1$, the block is in the stable state, large area casing deformation will not likely occur; if the water-affected region exceeds 50% and expands to more than 70%, the formation is in the elastic-plasticity stage with the value of $K < 1.68$, the stability becomes worse, it is the critical stage of casing deformation; if the water-affected region is larger than 70%, the block creeps and slides from the high pressure area along the soft structure plane to the lower pressure area.

Table 5-4: Water-affected Ratio and *K* under Fixed Injection Pressure and Pressure Difference

Water-affected Ratio (%)	*K*
0	0.23
30	0.38
50	1.00
70	1.68
100	1.71

If injection pressure is kept lower than 12.7 MPa and maintained stable, at the same time keeping the water-affected area ratio to a certain fixed value, how will block pressure differences influence the stability? Four regimes were devised; for each regime, a block pressure difference range of 0.00 to 2.40 MPa were used, and the simulation results are as follows (Table 5-5):

- Regime a, water-affected area is 0%, and under the block pressure difference range the formation will remain stable. The K value is very small. ($K \leqslant 0.18$).
- Regime b, water-affected area is 30%, and under the block pressure difference range the formation is still in a stable state. The K value is relatively small. ($K \leqslant 0.51$).
- Regime c, the water-affected area is 70%, and the formation is unstable. Casing shear is more likely to occur with a increase of block pressure differential.

- Regime d, water-affected area is 100%, the formation is unstable under the complete block pressure difference range, the simulation result is similar to regime c, and simple elastic-plastic theory is no longer suitable for such situations.

Table 5-5: Simulation Result of Regimes under Fixed Injection Pressure

Regime	Water-affected Ratio (%)	Block Pressure Difference (MPa)	*K*
A	0	2.40	0.18
		1.71	0.17
		1.10	0.17
		0.50	0.16
		0.00	0.16
B	30	2.40	0.51
		1.71	0.48
		1.10	0.45
		0.50	0.41
		0.00	0.39
C	70	2.40	2.03
		1.71	1.88
		1.10	1.73
		0.50	1.65
		0.00	1.56
D	100	2.40	2.04
		1.71	1.93
		1.10	1.77
		0.50	1.70
		0.00	1.64

From the above simulation results, it is observed that the water-affected area ratio influences the stability coefficient much more than block pressure differences. If the water-affected ratio is higher than 70%, stability coefficient values increase up to 0.5 or so when the block pressure difference changes from 0 MPa to 2.4 MPa. If the water-affected ratio is smaller than 30%, the stability coefficient value increases only 0.02-0.12 when block pressure difference changes from 0 MPa to 2.4 MPa. In order to further probe the phenomenon, some scenarios under injection pressure of 12.7 MPa and block pressure difference range of 0.0 to 2.5 MPa were executed. Table 5-6 lists the results of those scenarios. To maintain the large area casing stability under an injection pressure of 12.7 MPa and zero block pressure difference, the water-affected area ratio should be smaller than

52.3-60.5%, whereas if the injection pressure is 12.7 MPa and the block pressure difference is 2.5 MPa, the water-affected area ratio must be kept smaller than 48.2~53.5% to maintain areal casing stability.

Table 5-6 Simulation Result under Fixed Injection Pressure and Varied Block Pressure Difference:

Block Pressure Difference (MPa)	Water-affected Ratio (%)	*K*
2.5	<48.2~53.5	<1.0~1.2
2.0	<50.0~55.5	<1.0~1.2
1.5	<51.5~57.2	<1.0~1.2
1.0	<52.5~58.5	<1.0~1.2
0.5	<53.0~59.5	<1.0~1.2
0.0	<53.2~60.5	<1.0~1.2

5.6 Summary

Multi-period tectonic movements formed dense and complex distributions of faults in Daqing Oilfield. The fault blocks in the reservoir can have different formation pressures in the water injection and production activity. Block pressure difference is one of the key factors causing large area of casing shear. Also, because of the changing of stress field over geological time, most faults in the oilfield establish a "chair" shape. Local increase in thickness of formations near faults can be observed.

Far-field stress fields in Daqing Oilfield are a type of strike-slip fault regime. Relative magnitudes of stresses are $\sigma_H > \sigma_v > \sigma_h$ and the direction of major horizontal stress is N80°E.

Variation of injection pressure has obvious disturbance to the regional stress field. A pressure change of about 4 MPa can change the direction of casing displacement up to 65°, and can cause casing displacement magnitude change of 0.05 to 0.08 mm.

Numerical simulation results showed that variation of injection pressure could induce a substantial perturbation on the local stress field. Injection-induced stress fields overlap with the *in situ* stress field. Once the maximum compressive stress parallels or nearly parallels the

differential pressure, the stability of strata in shear is severely compromised, and when the thrust stress imposed exceeds the shearing resistance, the strata will slip in a direction corresponding to the vector from high pressure to low-pressure areas. The change in this creep and slip displacement field is the fundamental reason for the serious casing deformation damage in Daqing Oilfield.

Water content in the shale formation has an influence on rock shear resistance and a 5% increase of water content in shale in Daqing Oilfield can decrease the maximum shear resistance of shale by approximately 40% of the normal stress. The water-affected area contributes an important scale effect to large-area casing stability. The ratio of water-affected shale formation area influences the stability coefficient much more than block pressure difference. In the studied area under conditions of injection pressure of 12.7 MPa and no more than 2.5 MPa block pressure difference, the water-affected ratio should be smaller than 50% or so in order to maintain areal casing stability.

By history matching, in the studied area under current development conditions and water-affected ratio, so long as the injection pressure and pressure differential between blocks are controlled to be less than 12.7 MPa and 0.86 MPa respectively, formation shear slip along a horizontal surface will no longer occur.

Chapter 6
Summaries, Conclusions, and Future Work Recommendations

6.1 Summaries

Large area casing failure is always related to shear failure of rocks. Rock shear occurs when rock strength exceeds rock strength. Rock strength is not a constant: it is affected by numerous internal factors, such as grain size, mineral cement type, contact fabric, original cracks and fissures, anisotropy. Water saturation is an external condition that influences rock strength. The increased water saturation affects rock strength by decreasing both rock cohesion and rock friction angle, particularly in shale or at shale-sandstone interfaces. Water content in the shale formation thus has an influence on rock shear resistance. In subsurface conditions, higher water contents are correlated with higher pore pressures. Higher pressures mean lower effective stresses ($\sigma'_n = \sigma_n - p_f$), therefore high-pressure injection causes normal stress decrease and in turn lowers the maximum shear resistance. In Daqing Oilfield, a 5% increase of water content in shale can decrease the maximum shear resistance of shale approximately 40% of the normal stress.

Petroleum recovery activities, such as injection and production, cause pore pressure change and in turn influence porosity and stresses. Petroleum recovery activities of pressure increase or decrease can both induce casing shear. There are generally three typical forms of casing shear: horizontal shear at weak lithological interfaces within the overburden; horizontal shear at the top of a specific production or injection interval; and casing buckling and shear within the producing interval.

Reservoir heterogeneity is important to the understanding and the effective production of reservoirs. Reservoirs can contain impermeable lithological units and heterogeneous

porosity/permeability distributions that are further affected by complex fault systems. These can significantly affect fluid flow paths and distribution. Reservoir heterogeneity can be broadly classified as mega-heterogeneity, macro-heterogeneity and micro-heterogeneity. Macro-heterogeneity can be further divided into horizontal heterogeneity and vertical heterogeneity. Reservoir mega-heterogeneity and macro-heterogeneity are not too difficult to understand and characterize, and measures can be taken to mitigate the influence of the heterogeneity. Micro-level heterogeneities are not very easy to identify, and it is supposed that at the small scale they have no effect per se on casing shear.

Reservoir mega-heterogeneity in Daqing Oilfield is not severe with respect to the issues that affect casing shear because the geometry is simple and the large-scale structure is very flat with no more than a 6° limb dip angle. The complex multi-period tectonic movements formed a large number of complex distributed and chair-shaped faults in Daqing Oilfield, and the current far-field stress field in Daqing Oilfield reflects a strike-slip fault regime. Relative magnitudes of stresses are $\sigma'_H > \sigma'_v > \sigma'_h$. The direction of the major horizontal stress is N80°E. Faults are numerous and apparently evenly distributed, but no large-scale fractures and folds were found. Large area casing shear has no apparent relationship with mega-heterogeneity except that the numerous and complex faults may help in leading to inter-block pressure difference during injection-production operations.

Macro-heterogeneity is severe in Daqing Oilfield. Lithostratigraphy, structural styles, and facies architecture are the three fundamental heterogeneous elements. Horizontal heterogeneity is characterized by various different depositional facies which can then be subdivided into micro-facies such as channel facies, delta inner front facies, and delta outer front facies. Sand body geometries, distribution dimension and physical properties among the facies vary greatly. Vertical heterogeneity of Daqing Oilfield is characterized by up to 100 individual sand layers with thickness ranging from 0.2 meters to 20 meters and a permeability range from 20 to 1600 mD (average 230 mD). Furthermore, there are a number of stacked sand-silt-shale sequences.

The reservoir sandstones of Daqing Oilfield have similar porosities and mineralogies, and the micro-heterogeneity lies in a considerable variation in the micro-structure. The difference in micro-structure affects permeability, which therefore also varies considerably, and it also affects micro-scale anisotropy, which shows a strong directional dependence.

Combinations of mercury porosimetry and photo-micro-graphic analysis can lead to a better understanding of pore accessibility and pore structure characterization. By using the method, complete pore size distribution of a range of several nanometers to several thousands of micro-meters can be obtained. Also, cumulative pore volume distribution and pore-throat aspect ratio can be obtained. Fractal dimension can be used to describe the heterogeneity of pore structure; the larger the fractal dimensions of the pore structure, the more heterogeneous the pore structure is for the particular sandstone sample.

Pressure change can cause variation of pore porosity, permeability, and pore size distribution. Hysteretic behavior can be observed when increases in effective overburden stress take place, porosity and permeability will decrease but will not recover to initial values even when effective stress was lowered to initial levels. Pore size distribution under changed effective overburden stress evidences a shift of pore sizes toward smaller pore size direction when stress increases. Pore sizes distribution cannot recover to its initial level when stress decreases to initial state.

Reservoir geomechanics is about the simultaneous study of fluid flow and mechanical response of reservoirs. The multi-component nature of reservoir rock requires descriptions of both pore fluid and solid component. Fluid flow in deformable porous media can be described by governing equations for fluid flow and governing equations for solid deformation. Governing equations for fluid flow include the mass conservation equation and Darcy's law. Solid deformation is governed by the overall momentum balance equation. Constitutive relations for flowing fluids in porous media can be given by density relations. The constitutive equation for deformation of the solid phase can be given by a scaled-up stress-rheological model. Governing equations, constitutive equations, initial conditions, and appropriate boundary conditions in the discretized system provide an equation set. Primary

unknowns of the system are determined by numerical finite element process. Among the many different coupling techniques, iterative coupling method is used most because of its stability, accuracy, and modularity feature.

Variation of injection pressure has an obvious disturbance to the regional stress field. This phenomenon was observed through both numerical simulation and *in situ* experiments. A pressure change of about 4 MPa can change the direction of casing displacement up to 65°, and can cause casing displacement magnitude change of 0.05mm to 0.08 mm.

The water-affected area has a scale effect on large-area casing stability. The ratio of water-affected shale formation area influences the stability coefficient much more than block pressure difference. In the studied area under conditions of injection pressure of 12.7 MPa and no more than 2.5 MPa block pressure difference, the water-affected ratio should be smaller than 50% or so in order to maintain areal casing stability.

By history matching, in the studied area under current development condition and water-affected ratio, so long as the injection pressure and pressure differential between blocks are controlled to be less than 12.7 MPa and 0.86 MPa respectively, formation shear slip along a horizontal surface will no longer occur.

6.2 Conclusions

The thesis presents a methodology for semi-quantitatively determining or predicting large area casing shear occurrence. The method is based on physical analysis and hypothesis of the mechanisms, *in situ* measurements, geological modeling and numerical simulation of a coupled stress-flow system.

Three key factors can be used to account for the physics of large area casing shear occurrence in Daqing Oilfield Shear. They are changes in the shearing resistance of shale formations with increases in water content, great reservoir heterogeneity, and long periods of high-pressure water injection. It is observed that water content in the shale formation has an influence on rock shear resistance and a 5% increase of water content in shale in Daqing

Oilfield can decrease the maximum shear resistance of shale by approximately 40% of the normal stress magnitude. The influence of reservoir heterogeneity depends on the various scales of heterogeneity considered. Macro-heterogeneity and faults cause unevenly distributed formation pressure and therefore cause inter-block pressure differences. Hysteretic behavior causes porosity and permeability decreases after the compaction stage of oilfield development. The subsequent injection pressure was inevitably kept relatively higher than initial pressures, a policy driven by production rate goals in Daqing Oilfield.

It is supposed that injection-induced stress fields combine in an additive manner with the *in situ* stress field. Because of reservoir vertical heterogeneity, long-term high-pressure injection causes overburden shale formation water content to be affected. The affected area increases with time as high-pressure injection continues. The increased water saturation affects rock strength by decreasing both rock cohesion and rock friction angle. Also, high-pressure injection causes a normal effective stress decrease. Once the maximum compressive stress parallels or nearly parallels the differential pressure, and the water-affected shale area is big enough, the stability of strata in shear is severely compromised. When the thrust stress imposed exceeds the shearing resistance, the strata will slip in a direction corresponding to the vector from high-pressure to low-pressure areas. The changes lead to slip displacement and slow creep, and this displacement along the weak plane is the fundamental reason for the serious casing deformation damage in Daqing Oilfield.

In situ experiments verified that a pressure change of about 4 MPa can change the direction of casing displacement up to 65°, and can cause casing displacement magnitude changes of 0.05mm to 0.08 mm. Further simulation results gave the critical state of formation stability under condition of particular injection pressures, block pressure differences, and the water affected shale area ratio. From reservoir engineering and reservoir pressure points of view, the water-affected area should be controlled to be smaller than 50% of all the shale area involved. Once the water-affected area is larger, injection pressure and block pressure difference should be carefully monitored and controlled.

By using the methodology, the large area casing stability in one typical area was analysed. The original hypothesis was demonstrated to be reasonable, and the relative effect of several parameters (strength, area, pressure difference) clarified. Although the method was based on one of the most seriously casing sheared areas in Daqing Oilfield, it will be applicable for other areas with similar reservoir characteristics and properties.

6.3 Future Work Recommendations

Although we have, using reservoir geomechanics techniques, semi-quantitatively studied the large-area casing shear issue in Daqing Oilfield, more work should be done in a more highly quantitative manner in order to fully understand details of the issue in the whole oilfield. Directions of future research suggested by this work are:

The first thing is to develop methods to measure, monitor, or to estimate *in situ* stresses for wells at a large scale instead of only in several wells. Detailed reservoir geomechanics study requires abundant, accurate, and dynamic *in situ* stress information for more wells in the studied area. Perhaps high resolution 3-D seismic surveys combined with geomechanics simulation and hydraulic fracture measurements cold constrain the stress field changes adequately.

The second thing is to devise methods to simulate larger areas of the oilfield. Such a model will be able to incorporate many more layers, not only including the upper layers of the reservoir, but also the lower intervals that contain mostly production layers. This may require more powerful calculation hardware or software than is currently commercially available.

The third thing is to investigate further the preconditions for the iterative coupling technique, and this will entail both theoretical analysis and numerical tests, backed up by field data for validation in practice.

Nomenclature

a, b, c	= Coefficient for permeability with porosity and integrated autocorrelation function unit less
c_m	= Compressbility coefficient of rock matrix ms^2/kg
c_f	= Fluid compressibility ms^2/kg
c'	=Cohesion $kg/m{\cdot}s^2$, 1 Mpa=$10^6 kg/m{\cdot}s^2$
$\boldsymbol{D}$	= Accumulation matrix unit less
D	= Fractal dimension unit less
DIS	= Average casing displacement unit less
DIS_e	= Critical casing displacement when areal casing deformation will occur unit less
$\boldsymbol{E}$	= Flow matrix unit less
E	= Young's modulus $kg/m{\cdot}s^2$, 1 Mpa=$10^6 kg/m{\cdot}s^2$
$\boldsymbol{F}$	= Vector of force boundary conditions unit less
$F_s(Qr)$	=Form factor for a sphere of radius r unit less
$f(r)$	= Probability density of the pore size distribution unit less
f_w	= Water content %, unit less
g	= Gravity m/s^2
H	= Depth calculated from a certain datum plane, downwards positive m
h	= Rock thickness m
$I(Q)$	= Scattering intensity unit less
$\boldsymbol{K}$	= Stiffness matrix unit less
K	= Stability coefficient unit less
k	= Permeability m^2, 1 Darcy=$10^{-8} m^2$
k_0	= Initial permeability m^2, 1 Darcy=$10^{-8} m^2$
$\boldsymbol{L}$	= Coupling matrix to flow unknowns unit less
m	= Variation in fluid mass content kg
dm/dt	= Rate of change with time kg/s
N	= Lithologic constant unit less
$\boldsymbol{n}$	= Unit outward normal vector unit less
$\boldsymbol{P}$	= Vector of reservoir unknowns unit less
Δp	=Pressure draw down $kg/m{\cdot}s^2$, 1 MPa=$10^6 kg/m{\cdot}s^2$
p_f	= Fluid pressure $kg/m{\cdot}s^2$, 1 MPa=$10^6 kg/m{\cdot}s^2$
p_{f0}	= Initial fluid pressure $kg/m{\cdot}s^2$, 1 MPa=$10^6 kg/m{\cdot}s^2$
$\boldsymbol{Q}$	= Vector of boundary conditions unit less
Q	= Magnitude of the scattering vector unit less

$\boldsymbol{R}$ = Right hand side of flow equation unit less

R_{max} = Maximum pore radii m

R_{min} = Minimum pore radii m

r = Pore radius m

r_p = Pore size m

r_t. = Throat size m

r_p/r_t. = Pore-throat aspect ratio unit less

S_2(r) = Two-point correlation function unit less

S_{Hg} = Sample saturation to mercury unit less

V_p =Velocity of P wave m/s

V_r =Volume of a sphere of radius r m^3

$\boldsymbol{v}$ = Darcy's velocity vector unit less

v = Fluid macroscopic unit less

$\boldsymbol{T}$ = Symmetric transmissibility unit less

T = Temperature ℃

t = Time s

w = Source term unit less

Z(x) = Binary phase function unit less

α = Biot parameter unit less

ε = Overall strain velocity unit less

$\boldsymbol{\delta}$ = Vector of displacement unit less

φ = Internal friction angle degree

ϕ = Porosity %, unit less

η = Coefficient of rock viscosity unit less

θ = Rock structure variable unit less

μ = Fluid viscosity kg/m·s, 1 cp =10^{-3}kg/m·s

μ' =Friction coefficient unit less

ρ = Rock mass density kg/m^3

ρ_f = Fluid density kg/m^3

ρ_{f0} =Initial fluid density kg/m^3

ρ_m =Rock matrix density kg/m^3

$(\Delta\rho)^2$ = Scattering length density contrast unit less

σ = Stress $kg/m{\cdot}s^2$, 1 Mpa=10^6kg/m·s^2

σ_1 = *Maximum stress kg/m·s^2, 1 Mpa=10^{6}kg/m·s^2*

σ_2 = *Intermediate stress kg/m·s^2, 1 Mpa=10^{6}kg/m·s^2*

σ_3 = *Minimum stress kg/m·s^2, 1 Mpa=10^{6}kg/m·s^2*

σ_H = *Maximum horizontal stress kg/m·s^2, 1 Mpa=10^{6}kg/m·s^2*

σ_h = *Minimum horizontal stress kg/m·s^2, 1 Mpa=10^{6}kg/m·s^2*

σ_v = *Vertical stress kg/m·s^2, 1 Mpa=10^{6}kg/m·s^2*

σ_n = *Normal stress kg/m·s^2, 1 Mpa=10^{6}kg/m·s^2*

σ' = *Effective stress kg/m·s^2, 1 Mpa=10^{6}kg/m·s^2*

σ'_H = *Effective maximum horizontal stress kg/m·s^2, 1 Mpa=10^{6}kg/m·s^2*

σ'_h = *Effective minimum horizontal stress kg/m·s^2, 1 Mpa=10^{6}kg/m·s^2*

σ'_v = *Effective vertical stress kg/m·s^2, 1 Mpa=10^{6}kg/m·s^2*

σ'_n = *Effective normal stress kg/m·s^2, 1 Mpa=10^{6}kg/m·s^2*

τ =*Shear stress kg/m·s^2, 1 Mpa=10^{6}kg/m·s^2*

τ_{max} =*Maximum shear stress kg/m·s^2, 1 Mpa=10^{6}kg/m·s^2*

$\boldsymbol{\Omega}$ = *Domain of interest unit less*

References

Alpay O.A., 1972. A Practical Approach to Defining Reservoir Heterogeneity, Journal of Petroleum Technology. July(1972):841-848.

Amirtharaj E., Ioannidis M.A., and Macdonald I.F., 2003. Statistical Synthesis of Image Analysis and Mercury Porosimetry for Multiscale Pore Structure Characterization. SCA Paper 2003-10. In the proceeding of Annual Symposium of the Society of Core Analysts, Pau, France, Sept. 22.

Biot M. A., 1955. Theory of elasticity and consolidation for a porous anisotropic solid. Journal of Applied Physics, 26:182-185.

Biot M. A., 1956. Theory of deformation of a porous viscoelastic anisotropic solid. Journal of Applied Physics, 27:452-469.

Biot M. A., 1962. Mechanics of deformation and acoustic propagation in porous media. Journal of Applied Physics, 33:1482-1498.

Biot M.A., 1973. Nonlinear and semilinear rheology of porous solids. Journal of Geophysics Research, 78:4924-4937.

Biot M. A., and Willis D. G., 1957. The elastic coefficients of the theory of consolidation. Journal of Applied Mechanics, 24:594-601.

Chan A.W., 2004. Production-Induced Reservoir Compaction, Permeability Loss and Land Surface Subsidence. Ph.D. Thesis. Stanford University. California, U.S.A.

Chang D. and Ioannidis M.A., 2002. Magnetization evolution in network models of porous rock under conditions of drainage and imbibition. Journal of Colloid and Interface Science, 253:159-170.

Chen Q., Kinzelbach W., Ye C., and Yue Y., 2002. Variations of Permeability and Pore Size Distribution of Porous Media with Pressure. J. Environ. Qual. 31:500-505.

Chen Z., Meng Q., Wan T. Jia Q., and Zhang T, 2002. Numerical Simulation of Tectonic Stress Field in Gulong Depression in Songliao Basin Using Elastic-Plastic Increment Method (In Chinese). Earth Science Frontiers, 9(2): 483-492.

Da Silva, F.V., Debanda, G.F., Pereira, C.A. and Plischke, B. 1990. Casing collapse analysis associated with reservoir compaction and overburden subsidence. In Proceedings of SPE European Petroleum Conference, 21-24 October, The Hague, Netherlands, 127-134.

Dullien F.A.L., 1979. Porous Media Fluid Transport and Pore Structure. Academic Press, New York (1979) 127.

Dusseault M. B., Bruno M. S., and Barrera J., 2001. Casing Shear: Causes, Cases, Cures. SPE Drilling & Completion. (6): 98-107.

Dusseault, M.B., 2005. Rock Mechanics, Course notes, University of Waterloo.

Evans G.W. and Harriman D.W., 1972. Laboratory test on collapse resistance of cemented casing. In Proceedings of 47th Annual Fall Meeting of the Society of Petroleum Engineers of AIME. San Antonio, Tex.

Fredrich J. T., Arguello J. G., Deitrick G. L., and Rouffgnac E. P., 2000. Geomechanical modeling of reservoir compaction, surface subsidence, and casing damage at the Belridge diatomite field. SPE Reservoir Eval. and Eng., 3(4):348-359.

Fredrich J. T., Deitrick G. L., Arguello J. G., and Rouffgnac E. P., 1998. Reservoir Compaction, Surface Subsidence, and Casing damage: A Geomechanics Approach to Mitigation and Reservoir Management. SPE Paper 47284. In the proceeding of SPE/ISRM Eurock, Trondheim, Norway.

Gai X., Dean R. H., Wheeler M. F., and Liu R., 2003. Coupled geomechanical and reservoir modeling on parallel computers. SPE paper 79700, in the proceedings of the SPE Reservoir Simulation Symposium, Houston, Texas.

Ghaboussi J. and Wilson E. L., 1973. Flow of compressible Fluid in porous elastic media. International Journal of Numerical Methods in Engineering, 5:419-442.

Greenkorn R.A., and Haselow J.S., 1988. Unstable Flow in Heterogeneous Porous Media. SPE Paper 17114, in the proceedings of SPE/IADC Drilling Conference, Dallas, Texas.

Griffith, A. A., 1920. The phenomena of rupture and Ffow in solids, Philos. Trans. R. Soc. London Ser. A, 221, 163-198.

Guo W., Yan Y., Liu B., and Liu Q., 2000. Evaluation on Result of Multiple Infilling & Adjustment in Sazhong Area. SPE Paper 64748, In the Proceedings of SPE International Oil and Gas Conference and Exhibition. Beijing, China.

Han G., 2003. Rock Stability under Different Fluid Flow Conditions. PhD Thesis. University of Waterloo, Ontario, Canada.

Han H.X., Dusseault M.B., Xu B. and Peng B., 2006. Simulation of Tectonic Deformation and Large-Area Casing Shear Mechanisms - Part A: Operations. SPE Paper 100360, In the Proceedings of SPE Europec/EAGE Annual Conference and Exhibition, Vienna, Austria.

Han H.X., Dusseault M.B., Xu B. and Peng B., 2006. Simulation of Tectonic Deformation and Large-Area Casing Shear Mechanisms - Part B: Operations, ARMA 06-1004, In the Proceedings of The 41st U.S. Symposium on Rock. Golden, Colorado.

Han H.X., Ioannidis M., Dusseault M.B., Xu B. and Peng B., 2006. Multiscale Pore Structure Characterization By Combining Image Analysis And Mercury Porosimetry. SPE Paper 100353, In the Proceedings of SPE Europec/EAGE Annual Conference and Exhibition, Vienna, Austria.

Han H.X., and Liu H., 2000. Laboratory Measurement on Core Sample Supersonic Wave Rate and Attenuation Characteristics (In Chinese with English Abstract). Petroleum Explorationist, 5(4): 43-47.

Ibekwe I.A., Coker-III O.D., Fuh G.F., and Actis S.C., 2003. Magnolia Casing Design for Compaction. SPE Paper 79816. In the proceeding of the SPE/IADC Drilling Conference. Amsterdam, The Netherlands.

Ioannidis M.A., Kwiecien M.J., and Chatzis I., 1996. Statistical analysis of the porous micro-structure as a method for estimating reservoir permeability. Journal of Petroleum Science and Engineering, (1996), 16, 251-261.

Ioannidis M.A., Kwiecien M.J., Chatzis I., Macdonald I.F., and Dullien F.A.L., 1997. Comprehensive Pore Structure Characterization Using 3D Computer Reconstruction and

Stochastic Modeling. SPE Paper 38713. In the proceeding of SPE Annual Technical Conference and Exhibition, San Antonio, Texas.

Jenny P., Wolfsteiner C., Lee S., and Durlofsky L., 2002. Modeling Flow in Geometrically Complex Reservoirs Using Hexahedral Multiblock Grids. SPE Journal. June(2002):149-157.

Jha B., 2005. A Mixed Finite Element Framework for Modeling Coupled Fluid Flow and Reservoir Geomechanics. Msc Thesis. Stanford University. California, USA.

Lan Z., Xia Y., and Zhang C., 2000. The Repairing Technology of Driving Channel on Small Drifting diameter's Casing Damage in Daqing Oilfield. In Proceedings of the SPE International Oil and Gas Conference, Beijing, China.

Li Q., Wang Y., and Dong H., 1995. Relationship Between Reasonable Injection-Production Ratio and Pressure Level in Development Area of Southern Saertu Reservoir. SPE Advanced Technology Series. 1(5): 28-34.

Li Z., and Zhang J., 1997. *In situ* Stress and Petroleum Exploration &Development (In Chinese, with English Abstract). Petroleum Industrial Press. Beijing, P.R.China.

Liu H., Han H.X., Li Z., and Wang B., 2006. Granular-Polymer-Gel Treatment Successful in the Daqing Oil Field. SPE Production & Operations. 1 (21): 142-145

Liu H., Yang Y., Wang Q., Yan J., and Dang H., 2005. Challenges and Countermeasures Facing Casing Damage in Daqing Oilfield. In Proceedings of SPE Europec/EAGE Annual Conference, Madrid, Spain.

Liu H., Wan X., 1995. Development Adjustment of Heterogeneous Sandstone Reservoir at Late Period of High Water Cut Stage. SPE Paper 29949. In the Proceedings of SPE International Meeting on Petroleum Engineering. Beijing, China.

Lu X., Sui J., Zhao H., and Yang H., 2000. Stochastic Modeling Technique for Heterogeneous Multi-layer Sandstone Reservoir. SPE Paper 64764, In the Proceedings of SPE International Oil and Gas Conference and Exhibition. Beijing, China.

Ortoleva P., 1994. Geochemical self-organization. New York, Oxford University Press.

Osmar A., Moretti F. J., Cen M., and Yang Y., May 1990. Application of Geological Modeling and Reservoir Simulation to the West Saertu Area of the Daqing Oilfield. SPE Reservoir Engineering. 4 (5): 99-106.

Paterson L., Palnter S., Zhang X., and Plnczewskl W.V., 1998. Simulating Residual Saturation and Relative Permeability in Heterogeneous Formations, SPE Journal. September (1998): 211-218.

Peng B., Han H.X., and Li J., 2002. Permeability Prediction of the Three Dimensional Porous Media Through Flow Simulation Method (in Chinese with English Abstract). Petroleum Geology & Oilfield Development in Daqing Oilfield. 6(21): 19-21.

Radlinski A.P., Ioannidis M.A., Hinde A.L., Hainbuchner M., Baron M., Rauch H., and Kline S.R., 2002. Multiscale Chracterization of Reservoir Rock Micro-structure: Combining Small-Angle Neutron Scattering and Image Analysis. SCA Paper 2002-35. In the proceeding of Annual Symposium of the Society of Core Analysts, Monterey, California.

Radlinski A.P., Radlinska E.Z., Agamalian M., Wignall G.D., Lindner P., and Randl O.G., 1999. Fractal geometry of rocks" Physical Review Letters (1999) 82, 3078-3081.

Ruzyla K., 1984. Characterization of Pore Space by Quantitative Image Analysis, Paper SPE 13133 presented at the 1984 SPE Annual Technical Conference and Exhibition, Houston, Sept. 16-19.

Settari A., and Mourits F.M., 1998. A coupled reservoir and geomechanical simulation system. SPE Journal. Sept. 1998.

Settari A. and Walters D. A., 1999. Advances in coupled geomechanics and reservoir modeling with applications to reservoir compaction. In the proceedings of SPE Reservoir Simulation Symposium, Houston, Texas U.S.A.

Shen S., Miao P., and Watson A.T., 1992. Characterization of Pore Structure Using NMR-Restricted Diffusion Measurements. SPE Paper 24812. In the proceeding of SPE Annual Technical Conference and Exhibition, Washington.

Shen P., Li K., and Jia F., 1995. Quantitative Description for the Heterogeneity of Pore Structure by Using MercuryCapillary Presure Curves. SPE Paper 29996. In the proceeding of SPE International Meeting on Petroleum Engineering, Beijing, P.R.China, November 14-17.

Silva F.V., Debanda G. F., Pereira C. A., and Plischke B., 1990. Casing collapse analysis associated with reservoir compaction and overburden subsidence. In Proceedings of SPE European Petroleum Conference. The Hague, Netherlands, 21-24(10): 127-134.

Tan K., Xie Yanshi, Zhao Zhizhong, Li Xiaoming, 2001. Nonlinear Dynamics of Tectonic Mineralization: 1.An Incremental Stress Rheology Model. Geotectonica et Metallogenia (In Chinese, with English Abstract), (2001), 25, 381-388.

Tanzil D., Hirasaki G.J, and Miller C.A., 2002. Mobility of Foam in Heterogeneous Media: Flow Parallel and Perpendicular to Stratification, SPE Journal. June(2002):203-212.

Terzaghi K., 1943. Theoretical Soil Mechanics. Wiley, New York.

Thomas L.K., Chin L.Y., Pierson, and Sylte J.E., 2002. Coupled Geomechanics and Reservoir Simulation. SPE Paper 77723, in the proceedings of the Annual Technical Conference and Exhibition, San Antonio, Texas.

Thompson K.E. and Kwon O., 1999. Selective Conformance Control in Heterogeneous Reservoirs by Use of Unstable, Reactive Displacements. SPE Journal, 4(2):156-166.

Tortike W. S. and Ali S. M. 1987. A framework for multiphase non-isothermal fluid flow in a deforming heavy oil reservoir. SPE Paper 16030, in the proceedings of SPE Reservoir Simulation Symposium, San Antonio.

Ungerer P., Burrus J., Doligez B., Chenet P. Y., and Bessis F., 1990. “Basin evaluation by integrated two-Dimensional modeling of heat transfer, fluid flow, hydrocarbon generation, and migration”. AAPG Bulletin, (1990), 74, 309-335.

Wang D., Jiang C., and Sun Y., 1995. Major Technical Measures to Increase the Recoverable Reserves of Large Heterogeneous Sandstone Oilfields. SPE Advanced Technology Series. 1(5): 6-14.

Wang Y., and Liu H., 2004. How 50 Million Tons Annual Production Has Been Maintained For 27 Years In Daqing Oilfield. SPE Paper 87048, In the Proceedings of SPE Asia Pacific Conference on Integrated Modeling for Asset Management. Kuala Lumpur, Malaysia.

Wang Y., and Lu B., 2001. A Coupled Reservoir-Geomechanics Model and Applications to Wellbore Stability and Sand Prediction. SPE Paper 69718, in the proceedings of SPE International Thermal Operations and Heavy Oil Symposium, Margarita, Venazuela.

Whiteker S., 1966. The Equation of Motion in Porous Media, J. Amer. Inst. Chem. Eng., (1966) 29.

Yan J., Dang H., Ding H., and Wang H., 2005. The Development Technology of Non-Homogeneous and Multi-layer Sandstone Reserve in Daqing Oilfield. SPE Paper 92293, In the Proceedings of SPE Europec/EAGE Annual Conference. Madrid, Spain.

Yukler M. A., Cornford C., and Welte D. H., 1978. one-Dimensional model to simulategeologic, Hydrodynamic, and thermodynamic development of a sedimentary basin. Geol.Rundschau, (1978), 67: 960-979.

Zhang D., Li L., and Tchelepi H.A., 2000. Stochastic Formulation for Uncertainty Analysis of Two-Phase Flow in Heterogeneous Reservoirs. SPE Journal, 5 (1): 60-70.